Transportation Geotechnics 34 (2022) 100693

Contents lists available at ScienceDirect

Transportation Geotechnics

journal homepage: www.elsevier.com/locate/trgeo

A systematic framework for DEM study of realistic gravel-sand mixture from particle recognition to macro- and micro-mechanical analysis

Ruidong Li [a], Xiangyu Hu [a], Fan Chen [b], Xiang Wang [a,*], Hao Xiong [c,*], Hao Wu [d]

[a] Department of Civil and Environmental Engineering, The Hong Kong Polytechnic University, Hung Hom, Kowloon, Hong Kong, China
[b] Key Laboratory of Transportation Tunnel Engineering of the Ministry of Education, Southwest Jiaotong University, Chengdu 610031, China
[c] College of Civil and Transportation Engineering, Shenzhen University, Shenzhen 518060, China
[d] School of Civil Engineering, Central South University, 22 South Shaoshan Road, Changsha 410004, China

ARTICLE INFO

Keywords:
Gravel sand mixture
Particle shape
Deep learning
DEM simulation

ABSTRACT

Reproducing realistic particle shape is vital for discrete modeling of granular construction materials, such as sands and gravels, which are widely used foundation soils in civil engineering. The existing algorithms used to determine particle shapes from the raw images of construction materials are very limited, especially when dealing with binary mixtures, such as sandy gravel. To address this issue, this study aims to develop a systematic framework for realistic simulation of the gravel-sand mixture based on deep-learning-enhanced discrete element method (DEM). An efficient and convenient method is proposed to quickly identify particle contour and establish particle shape libraries based on a combination of YOLOv5 and U-Net algorithms. Furthermore, DEM-based biaxial compression tests are conducted on two groups of gravel-sand mixture based on the acquired realistic coarse and fine particle shapes. The influences of coarse particle shapes and fine sand content on the macroscopic and microscopic behaviors of gravel-sand mixtures are quantitatively and comparatively studied. The proposed framework for deep-learning-enhanced particle shape acquisition and realistic DEM simulation will provide researchers with more convincing physics-based insights into granular mechanics and has the potential to be extended into 3D to benefit practical problems.

Introduction

The gravel-sand mixture (GSM) is a highly heterogeneous loose geomaterial with a certain rock content that has existed since the Quaternary period. It is composed of rock with high strength, fine-grained soil, and pores. Not only is GSM a type of common geotechnical body found in nature, but it is also a unique geological body frequently encountered in various engineering constructions. However, due to the intricacy of the genesis formation and internal structure of GSM, its mechanical characteristics exhibit a high degree of variability and discontinuity, which is more complicated than that of homogenous soils or rocks [23,32,43]. In other words, even GSMs of the same origin and region may exhibit considerable variations in their *meso*-structure at various spatial locations, which will definitely have a detrimental effect on infrastructure safety [24,52]. Indeed, the *meso*-structural characteristics of GSM, to a large extent, control its *meso*-damage mechanism and macroscopic mechanical behavior characteristics under external loadings. Based on the *meso*-structure of GSM, the investigation of its *meso*-damage mechanism, deformation failure mechanism, and macroscopic mechanical characteristics will considerably deepen the theoretical system of gravel-sand mixture mechanics [47,60,67]. However, given the limitations of testing techniques, it is difficult to study the *meso*-mechanics, microslip displacement, and microscopic failure mechanisms of geotechnical materials with existing laboratory procedures [20,30,36,48].

In recent years, the discrete element method (DEM) has been demonstrated as an effective tool for better understanding mechanical behaviors of loose geotechnical materials from a *meso*-mechanical point of view [2,6,41,44]. In geotechnical engineering, DEM is widely used to study the failure of geo-structures and microscopic behaviors of samples in conventional geotechnical tests [1,44,46,56,63,66]. For example, the distinct structure of binary mixtures such as GSM, composed of coarse and fine particles with different particle characteristics (e.g., shape, size, and orientation), is critical, significantly affecting their mechanical response. The effects of these factors on the micromechanical behavior of the mixture are not easy to determine with laboratory experiments

* Corresponding authors.
E-mail addresses: xiang.wang@polyu.edu.hk (X. Wang), xionghao19529@szu.edu.cn (H. Xiong).

https://doi.org/10.1016/j.trgeo.2021.100693
Received 19 July 2021; Received in revised form 13 October 2021; Accepted 17 November 2021
Available online 20 November 2021

but are more accessible with DEM. Therefore, many studies have analyzed how these particle characteristics affect the mechanical behaviors of binary mixtures. According to Wang et al. [55], the shape of block stone significantly influenced the strength, friction energy, and shear band shape of the soil–rock mixture. Ng et al. [37] found that the peak shear strength of binary mixture is affected more by particle shape than by fine content. In addition, the majority of the constitutive parameters were demonstrated to be influenced by particle shape and can be correlated with a simple shape descriptor of sphericity [38]. These observations have motivated more studies on the influence of shape on the mechanical behavior of these binary mixtures, which also demonstrated the importance of shape in DEM simulation [8,17,21,39,65]. To better understand the mechanical behavior of GSM, DEM simulations of GSM with realistic particle shapes are needed. Some shape acquisition techniques, such as X-ray tomography, have been employed by other researchers [22,59,74]. Although 3D simulation is able to give more accurate and realistic results than 2D methods, the 3D modeling of realistic particle morphology results in much higher computational costs [57,58,72], Zhou et al. [73]. The 2D method reserves its advantages in revealing the physical insights and evolution laws of the macro- and micro-mechanical quantities for theoretical research studies. To address this, a method that reconstructs aggregate particle shape using the inverse Fourier transforms considering a limited number of significant harmonics was proposed [61]. For the extraction of bonded-particles, Spettl et al. [50] proposed a novel method to automatically represent sphere-like primary particles as exactly one (perfect) sphere, which can be used as input for DEM simulations. Furthermore, Liang et al. [28] proposed a particle shape extraction and evaluation method using a deep convolutional neural network and digital image processing, which was applicable for shape extraction of the gravel-sand mixture. However, these methods have several limitations, such as a limited application field, being time-consuming, or only being able to specific particles.

To address the problems stated above, this paper aims to propose a systematic framework for the DEM study of realistic GSM from particle recognition to macro-and micro-mechanical analysis, providing a novel perspective for analyzing GSM. First, a cost-effective close-range photogrammetry technique was employed to obtain high-resolution images of GSM samples. These raw images containing coarse and fine particles were then processed by YOLOv5 to compute the bounding boxes of each identified foreground particle automatically. Then, within each bounding box, the particle contour was extracted by the U-Net network. The shape indexes for each particle were evaluated, and all the information was stored in a shape database. Next, the coarse and fine particles chosen from the shape databases were employed to generate numerical samples of realistic gravel sand mixture in DEM simulations. Finally, biaxial compression tests were conducted on two groups of gravel-sand mixture with two types of coarse particles (ballast and cobble) and different sand content to investigate the effects of coarse particle shapes and fine sand content on macro- and micro-mechanical properties of GSM.

Particle identification and geometry quantification

This section aims to rapidly identify and extract the contours of fully projected coarse and fine particles from the full-size raw image of GSM samples as well as to build shape libraries based on the statistical analysis of elongation, angularity, and roughness.

Image acquisition based on close-range photogrammetry

Sample acquisition of GSM

This study employed ballast-sand mixtures (BSM) and cobble-sand mixtures (CSM) to be the GSM samples. All GSM samples for this investigation were obtained in Lanzhou, Gansu Province, China. To ensure the sample obtained was sufficiently preserved, the technique recommended by Geoguide 2 was used [42]. According to the guide, the sample was cut manually with a specialized cutter from material exposed in trial pits and excavations, which was completed immediately to avoid excessive moisture loss. After excavating from the soil, the undisturbed block samples were wrapped in grease-proof paper and coated with a series of layers of microcrystalline wax. Finally, as illustrated in Fig. 1, the sample was transported to the laboratory.

Implementation of close-range photogrammetry

The close-range photogrammetry scheme mainly consisted of establishing an automatic photographic system, image acquisition along a designated route, and image post-processing (Fig. 2).

As illustrated in Fig. 3a, the automatic photographic system consisted of a small four-axis gantry palletizing manipulator (SFGPM), digital camera, and computer. The camera is attached to the moving end of the SFGPM, which was controlled by a program. Before being photographed, the sample was placed in the center of the platform in the SFGPM. It is noted that the sample was contained in a detachable box placed in the center of the platform consisting of four bottomless wooden boxes and one wooden box with a bottom with the same dimension (Fig. 3b). Once the camera had finished the whole shooting procedure along the designated route, the top wooden box and the GSM within it were removed, and the shooting operation repeated. In this way, five GSM images were obtained with the same sample, which considerably improved the efficiency of image acquisition. Note that a 15 cm $\times$ 15 cm calibration board was adopted and positioned in the center of the sample surface to establish a local coordinate system that provided reference points for aligning photos and error reduction in image post-processing (Fig. 3c). The black squares with red flags on the calibration board were chosen as the reference points of the coordinate system (Fig. 3d). Point 1 represents the origin, whereas point 2 and point 4 are the positive directions of the X-axis and Y-axis. Moreover, point 3 serves as an error minimization control point.

When shooting along the designated route, an indispensable condition was to guarantee that adjacent images had enough overlapping area. To control the overlapping area, a grid layout in the camera was used to divide the whole image into 3 $\times$ 3 sections (Fig. 4a). An image was taken each time the camera moved a small section length (width) horizontally (vertically) along the shot route. Thus, every shot shared two-thirds of its image with an adjacent shot: the vertical middle third of the photo is the left (right) third of the next image, and the horizontal middle third of the photo is the top (bottom) third of the next image (Fig. 4b). For image post-processing, the commercial software Agisoft Photoscan [27] was used. The sparse point cloud was built based on the aligned images first. Then a dense point cloud was created based on

Fig. 1. Sample acquisition.

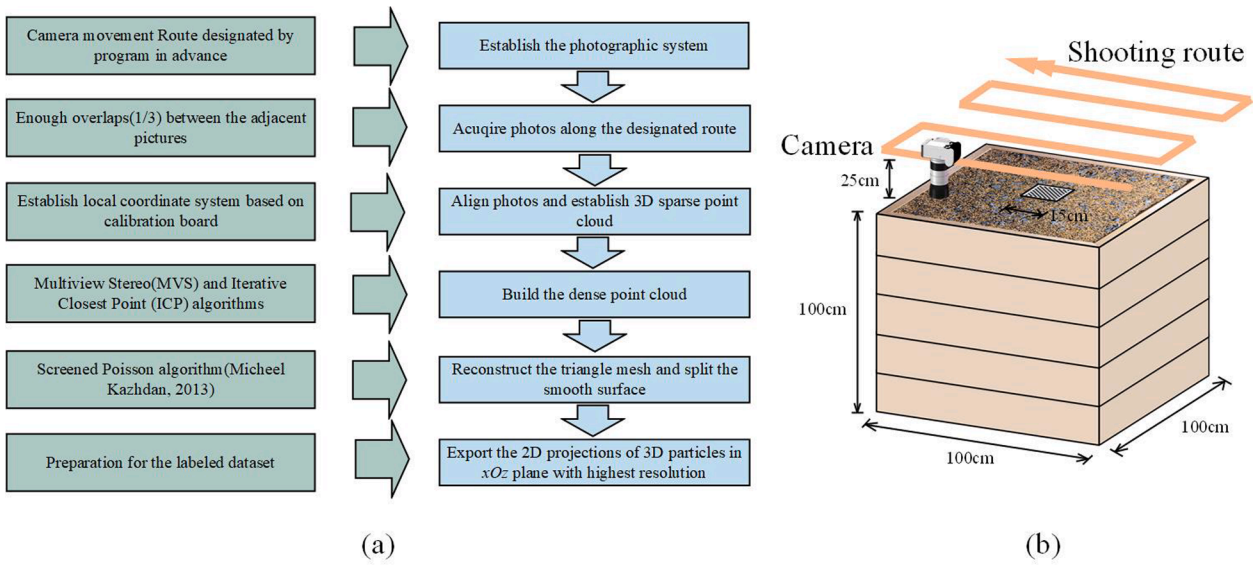

Fig. 2. The workflow and schematic diagram of close-range photogrammetry: (a) workflow of close-range photogrammetry, (b) schematic diagram of image acquisition.

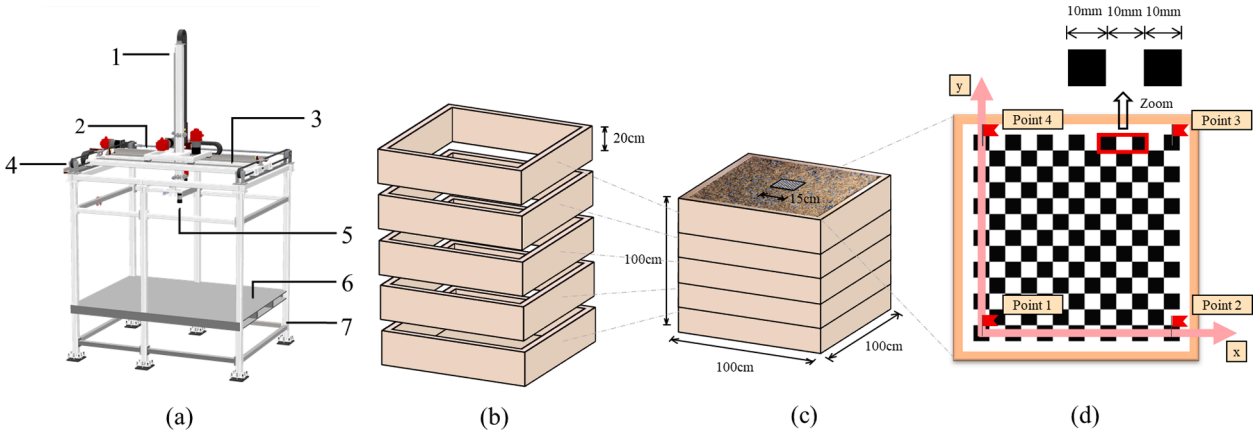

Fig. 3. Component of the automatic photographic system: (a) SFGPM, (b) detachable wooden boxes; (c) sample in wooden boxes; (d) establishment of the local coordinate system.

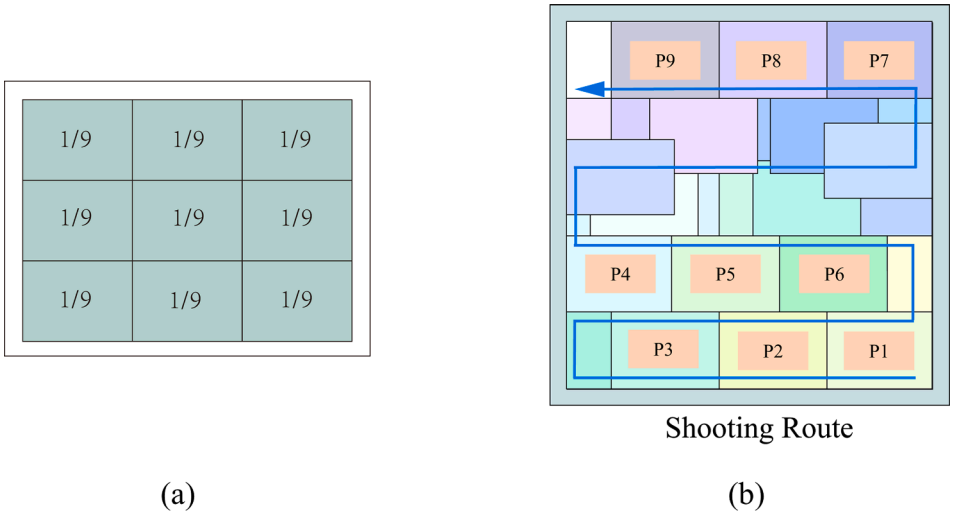

Fig. 4. The schematic diagram of shooting route: (a) camera grid lines, (b) schematic diagram of controlling overlaps between adjacent images.

multi-view stereo (MVS) algorithms [13,49]. Finally, the software fixed the textures, and the 2D projections of 3D GSM were outputted to an image with the highest resolution.

Computer-vision-based extraction of coarse and fine particle geometry

Detection of coarse and fine particle position

The prevalent object detection is divided into two parts: localization and classification. It begins by extracting the particular features such as Haar-like features [29] and HOG [35] before classifying the object by a localizer or classifier. Generally, these localizers and classifiers run over an image based on the region proposal approach or in-sliding window technique [14]. Following that, post-processing is utilized to eliminate duplicate bounding boxes. The techniques used in these methods are difficult to optimize and very complicated since each component is trained individually. However, systems like YOLO have reformed object detection as a one-step, single-regression problem by unifying a single network, which accelerates the speed of identifying objects.

This study adopted the latest YOLO version, YOLOv5 (Jocher et al., 2020), to detect coarse particles and sand in GSM. Compared with the last version of YOLOv4 [4], YOLOv5 reduces the weight file by nearly 90%, indicating that it is suitable for deploying embedded devices implement real-time detection. The object detection architecture of YOLOv5 has comprised of three parts: a pre-trained Backbone, a Neck, and a Head. As illustrated in Fig. 5, the input image features are compressed using a feature extractor (Backbone) and then given to the object detector (including the Neck and the Head). The Neck serves as a feature aggregator, collecting and blending the features generated in the Backbone for the Head phase [26]. Once YOLOv5 has located the object in the image, it generates a bounding box with the estimated accuracy rate around the object.

To detect ballast, cobble, and sand particles in images, three independent data sets: Y_ballast, Y_cobble, and Y_sand were created. Each set contained 600 images (400 for training, 100 for validation and 100 for test) obtained from part 2.1. In addition, the aspect ratio of the images was set 1:1 to avoid lossy training due to dimensional variations. The models were trained using a desktop on Nvidia GeForce RTX 3080 GPU having 10 GB of RAM. Learning rates for all the models were initialized to 0.001, and it was set to depreciate every 1,000 steps. All models were trained for 80 epochs, each dataset consisted of 400 training images and the batch size was set to 8. After training, the weight file of the recognition model obtained was saved, and the test set was utilized to evaluate the performance of the model.

The train loss and validation loss curves for Y_ballast, Y_cobble, and Y_sand are shown in Fig. 6, indicating that the loss value decreased rapidly in the first 20 epochs of network training and stabilized after 50 epochs. All losses were less than 0.03, which indicates the model trained well.

Furthermore, the evolution of mAP@0.5 (mean average precision, IoU = 0.5) and precision for three sets were plotted in Fig. 7a. The mAP@0.5 represents the mean AP (average precision) of all photos for all categories in the training set when IoU equals 0.5 [71]. As for IoU, it is an evaluation indicator for the accuracy of the predicted bounding box, representing the overlap degree between the prediction bounding box and the actual bounding box. As shown in Fig. 7a, mAP@0.5 and precision of ballast, cobble and sand were >0.88, demonstrating that the further prediction of models was accurate and reliable. The best weight recommended by YOLOv5 was adopted for detection, and the results are shown in Fig. 7b. It is distinct that the ballast, cobble, and sand particles are detected well from the image by those trained models. Therefore, a series of images were input into those models and correct results were stored in data sets D_ballast, D_cobble, and D_sand, respectively.

Extraction of particle contours

For extraction of particle contours, the U-Net [45] model was adopted. By classifying each pixel of the image, the U-Net model can achieve higher segmentation accuracy in less time than other methods while supporting training models with a small amount of data [70]. As illustrated in Fig. 8a, it consists of a contracting path (left side) and an expansive path (right side). Both paths are executed by some basic operations: (1) convolution (Conv), (2) max-pooling (MaxPool), and (3) up-convolution (UpConv). The Conv operation is the core part of the convolutional neural network; it typically extracts features from the input data (the black portion in Fig. 8b, which contains P_{11},$P_{12}\cdots P_{ij}$) and abstracts the implicit correlations in the original data through a convolutional kernel matrix. To avoid discarding the original image data and to retain the feature map the same size as the original image, a padding operation must be performed before the Conv operation, i.e., adding zeros along the perimeter of the original matrix to generate an extended input matrix. Following that, the kernel slides in regular stride ($S = 1$) along both the x and y axes and multiplies the elements at each place of the kernel by the corresponding elements in the input matrix, then sums them and adds a bias. Finally, the calculated value is written to the corresponding location of output (y_{ij}). This operation is as follows:

$$y_{ij} = AF\left(\sum_{m=i-s}^{i+s}\sum_{n=j-s}^{j+s}(x_{mn}w_{mn} + b)\right) \tag{1}$$

$$s = k_n/2 \tag{2}$$

where k_n is the size of the kernel matrix; x_{mn} is the element at position (m,n) of the input matrix, w_{mn} is the element of the nuclear matrix overlapping with x_{mn}, b is the bias term of the output feature graph, and $AF(\cdot)$ is the activation function. During the training process, both parameters w_{mn} and b are the targets of training. The default value of k_n is 3 and the default activation function is *ReLU* in this study.

The maxpool and upconv operations use different kernels and computations to down-sample and up-sample the input matrix, respectively. However, they are both executed by sliding windows, just like convolution operations. In this study, the maxpool operation can be considered as a special convolution operation, with $k_n = 2$ and $S = 2$, and the function of the formula y_{ij} is to output the maximum element covered by

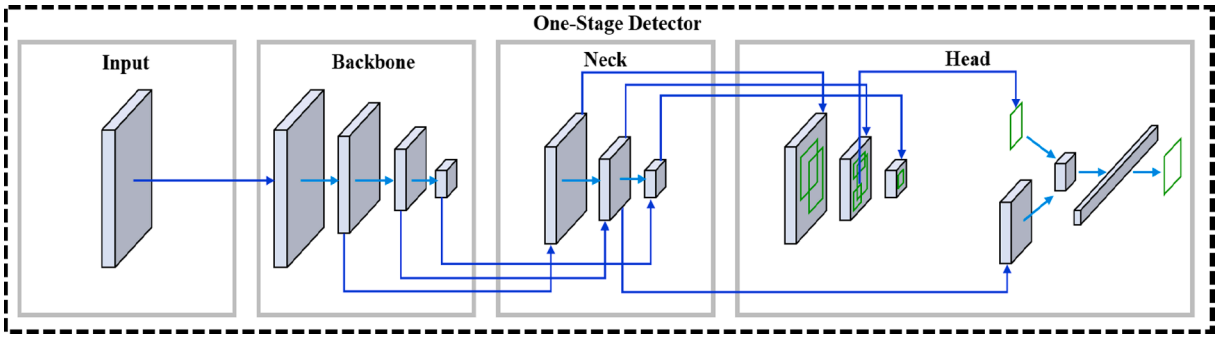

Fig. 5. Object detection architecture of YoloV5.

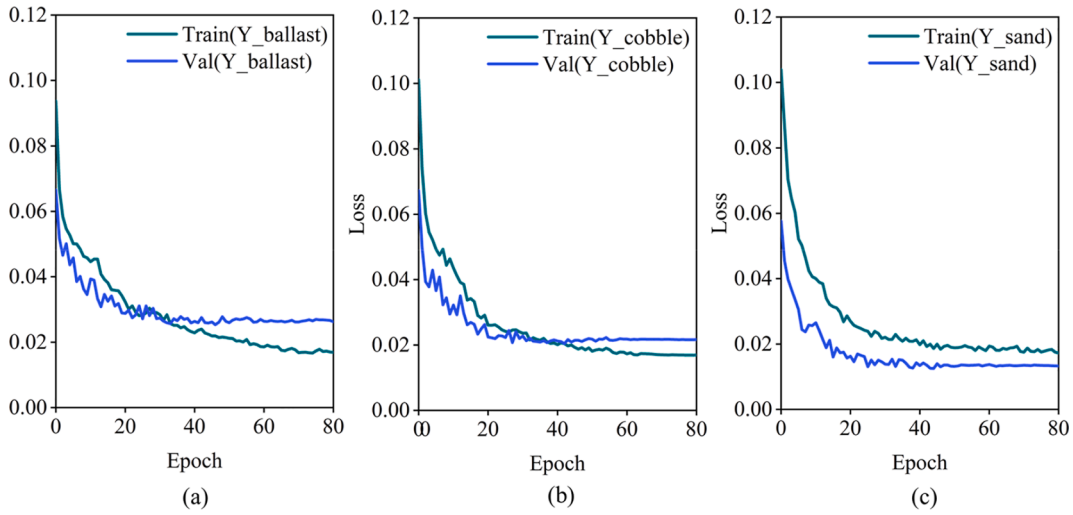

Fig. 6. Train loss and validation loss curves for three data sets: (a) Y_ballast, (b) Y_cobble, (c) Y_sand.

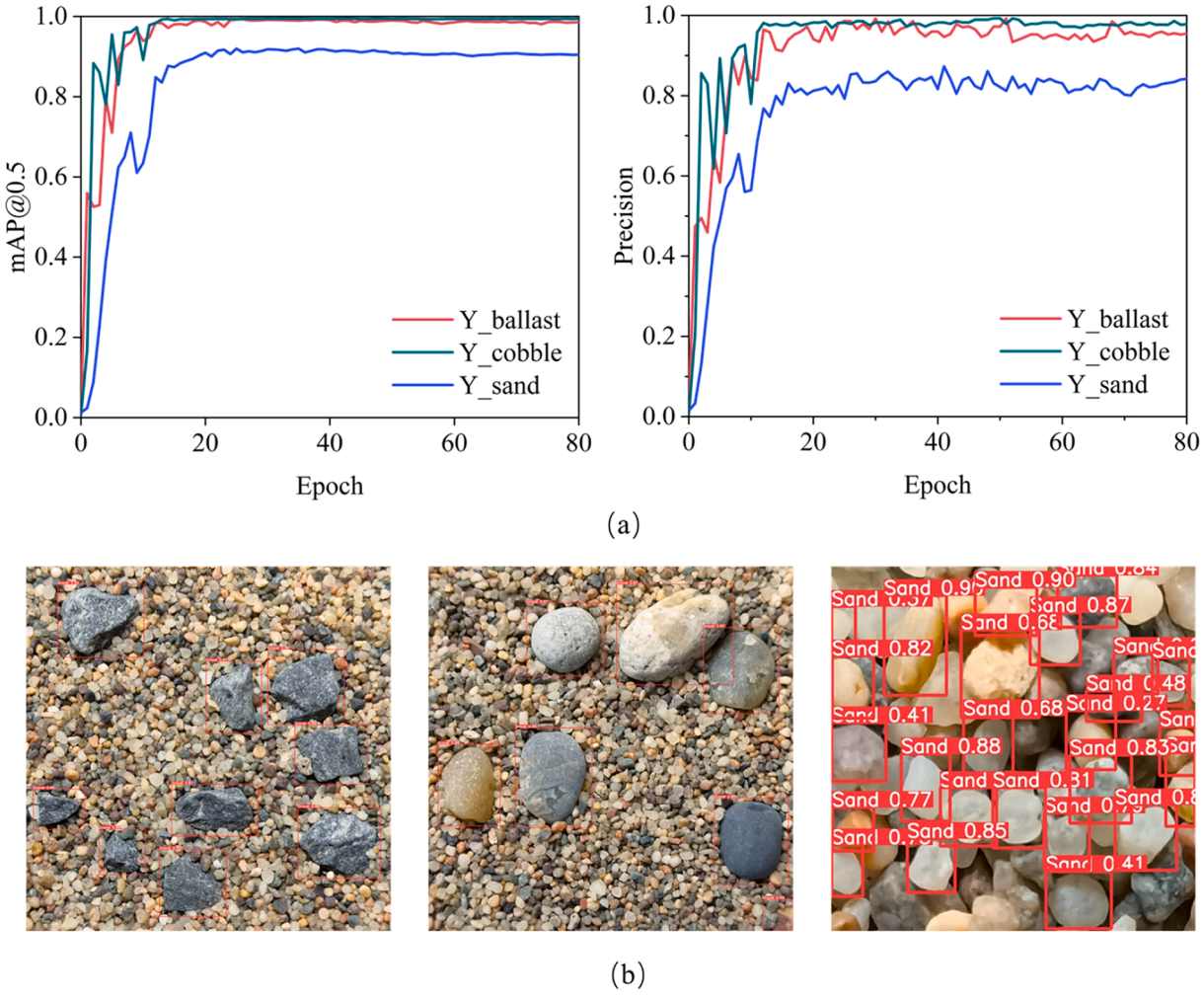

Fig. 7. Precision curve and detection results: (a) mAP@0.5 and precision curves (b) detection results.

the kernel. The upsampling operation is carried by using the keras-built upsampling2D. The loss function is chosen to be the weighted binary cross-entropy (WBCE) function [10]. The ADAM [25] optimizer is used to dynamically alter the learning rate of each parameter to minimize the loss function.

The images in sets D_ballast, D_cobble, and D_sand were imported into the U-Net model and the identification results of ballast, cobble, and sand were illustrated in Fig. 9, which indicated that the particle contours are well-identified from the background. Therefore, by employing the U-Net model, three databases U_ballast, U_cobble, and U_sand, contain 768

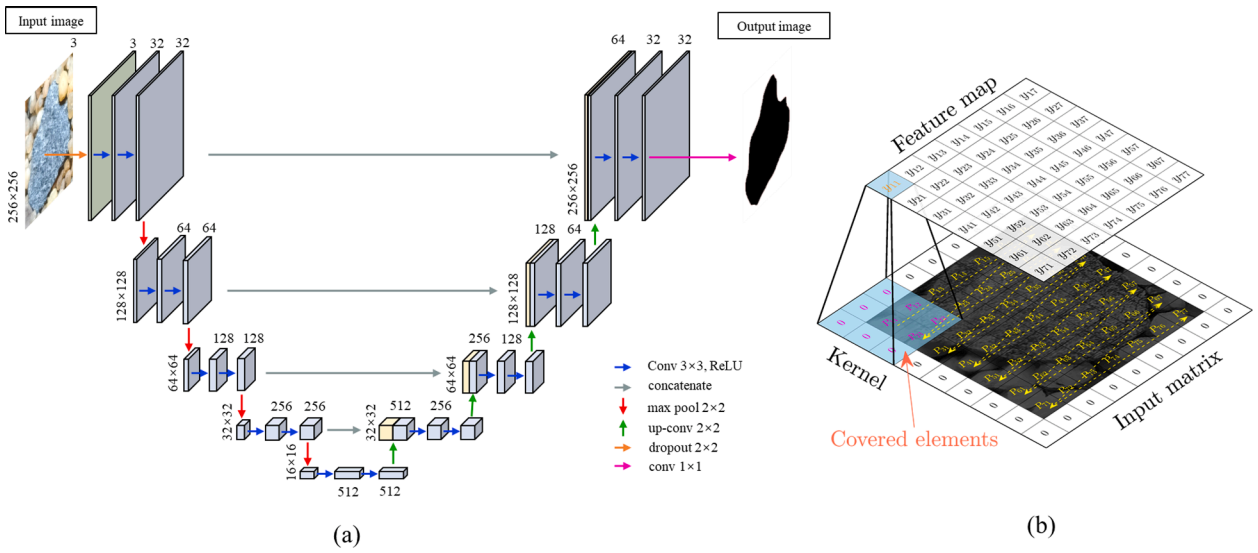

Fig. 8. The architecture of U-Net: (a) improved overall U-Net architecture, (b) convolution operation.

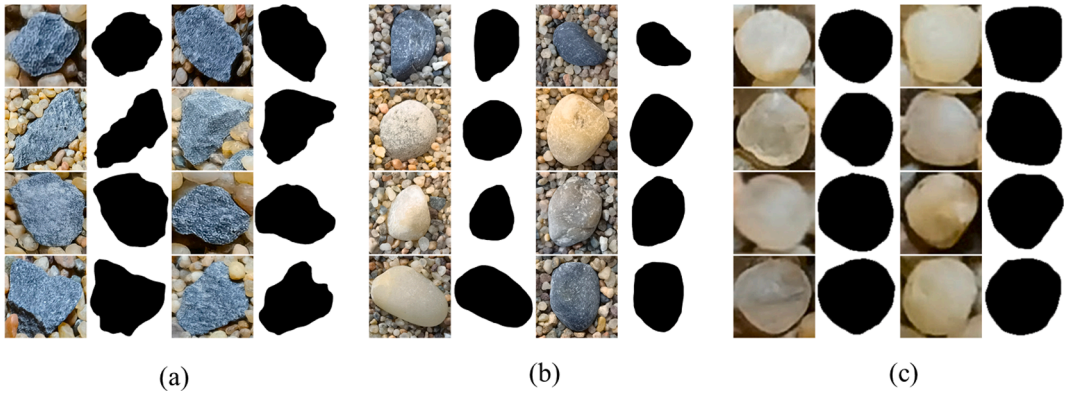

Fig. 9. Particle identification results: (a) U_ballast, (b) U_cobble, (c) U_sand.

ballast particle contours, 753 cobble particle contours, and 3820 sand particle contours, were established, respectively.

Particle geometry quantification and database establishment

Quantification of coarse and fine particle geometry

To quantify shapes in databases U_ballast, U_cobble, and U_sand, some shape indexes (e.g., elongation, angularity index, and roughness) are selected for analysis in this section [3].

(1) Elongation

The elongation (*EI*) is a frequently-used shape index for evaluating the particle contour [51]. The definition of *EI* is shown below:

$$EI = \frac{D_{minor}}{D_{\text{major}}} \tag{3}$$

where D_{minor} denotes the width along the minor principal axis and D_{major} denotes the length along the major principal axis. A higher *EI* value indicates that the particle is less thin. The two principal axes are determined by a second-order tensor matrix based on the normal vector of the particle contour (Eq. (4)).

$$\begin{cases} \Omega_{ij} = \dfrac{1}{L_p}\sum_{k=1}^{n} l^k T_i^k T_j^k \\ C = \begin{bmatrix} \Omega_{11} & \Omega_{12} \\ \Omega_{21} & \Omega_{22} \end{bmatrix} = \begin{bmatrix} cos\theta & -sin\theta \\ sin\theta & cos\theta \end{bmatrix} \begin{bmatrix} \lambda_a & 0 \\ 0 & \lambda_b \end{bmatrix} \begin{bmatrix} cos\theta & sin\theta \\ -sin\theta & cos\theta \end{bmatrix} \end{cases} \tag{4}$$

where T_i^k is the component of the unit normal vector T_k and of the *kth* micro-arc in *i* direction, and T_j^k represents the counterpart in *j* direction. L^k is the length of the *k*th micro-arc, L_P denotes the perimeter of the particle contour, which is the sum of lengths of *n* micro arcs (Fig. 10a). λ_a and λ_b are eigenvalues of matrix *C*. The value of λ_b is the minimum percentage of the arc length in particle contour perimeter along the major principal axis direction of Ω_{ij}, while the value of λ_a is the maximum percentage along the minor principal axis direction of Ω_{ij}. D_{minor} and D_{major} can be determined in a rectangle boundary enclosing the particle contour using two principal axis directions (Fig. 10b).

(2) Angularity index

Angularity index (*AI*) is defined by the sum of the distance difference between the contour of the particle and the contour of an equivalent ellipse [31]. Based on Fourier series analysis, a circle with the same perimeter as the original particle is first established as a benchmark for quantifying *AI*. The point on the particle outline can be mapped into this

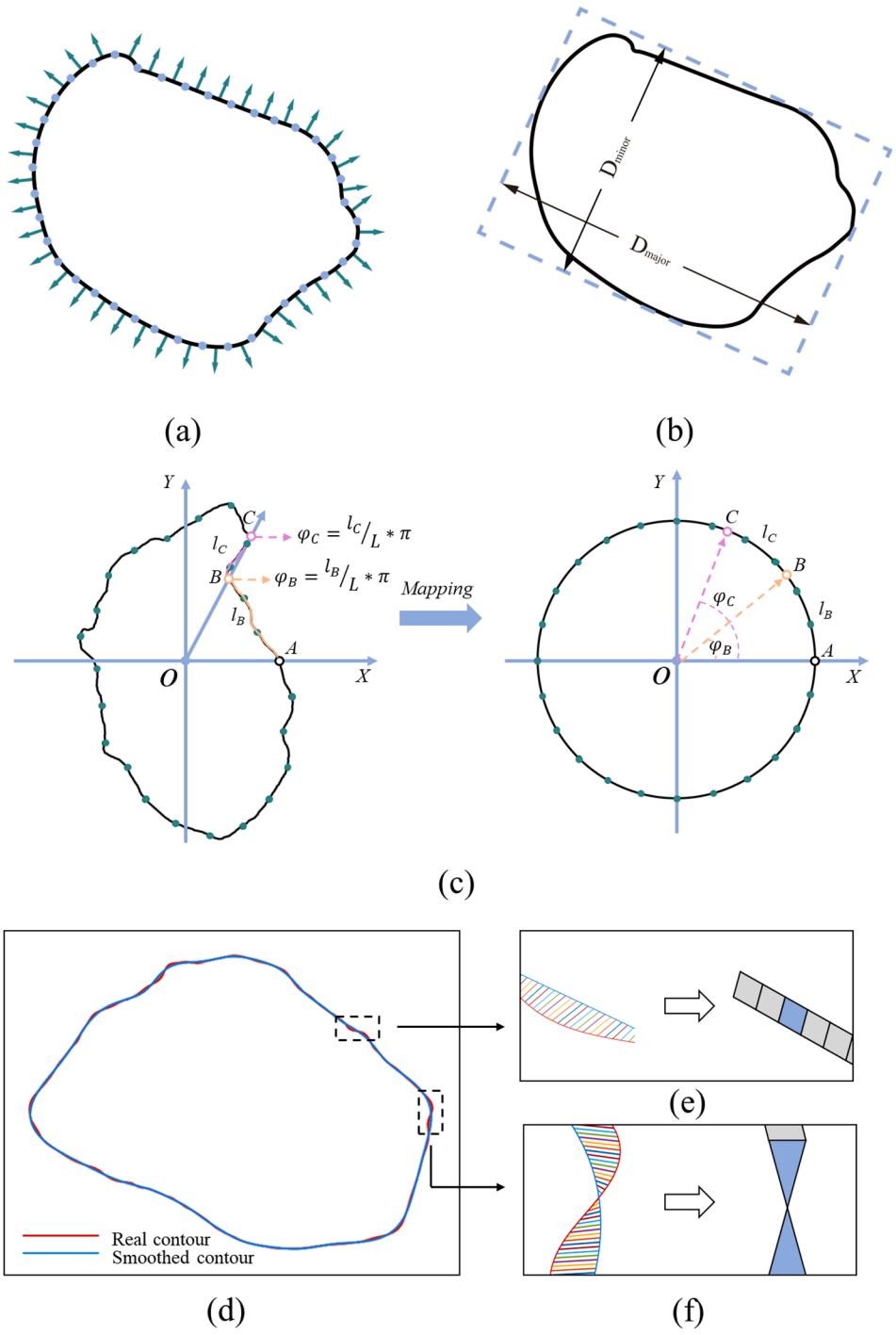

Fig. 10. Illustration of shape indexes; Elongation: (a) micro arc and the unit normal vector T_k, (b) rectangular box surrounding the particle contour; Angularity index: (c) benchmark contour of particles by Fourier analysis; Roughness: (d) smooth contour and real contour of a particle, (e) a simplified model of a quadrilateral deviation region, (f) a simplified model of a triangular deviation region.

circle and determined by a polar angle and a starting point (Fig. 10c). Then by Fourier series analysis as shown in Eqs. (5) and (6), the coordinates of points on the particle can be expressed by polar angle $\varphi^{'}(0 \le \varphi^{'} < 2\pi)$:

$$x(\varphi^{'}) = a_{x0} + \sum_{n=1}^{N}[a_{xn}cos(n\varphi^{'}) + b_{xn}sin(n\varphi^{'})] \tag{5}$$

$$y(\varphi^{'}) = a_{y0} + \sum_{n=1}^{N}[a_{yn}cos(n\varphi^{'}) + b_{yn}sin(n\varphi^{'})] \tag{6}$$

where x and y are coordinates of the boundary points, n denotes the serial number of harmonics, and N is the total number of harmonics. a_{x0}, a_{y0}, a_{xn}, a_{yn}, b_{xn}, and b_{yn} are Fourier coefficients. Thus, the gradient direction of boundary points is:

$$\theta = arctan\left[\frac{y^{'}(\varphi^{'})}{x^{'}(\varphi^{'})}\right] \tag{7}$$

where $x^{'}(\varphi^{'})$ and $y^{'}(\varphi^{'})$ are the derivatives of $x(\varphi^{'})$ and $y(\varphi^{'})$, and θ is measured from x-axis. Then, Eqs. (5) and (6) can be transformed as follows:

$$x^{'}(\varphi^{'}) = \sum_{n=1}^{N}[-na_{xn}sin(n\varphi^{'}) + nb_{xn}cos(n\varphi^{'})] \tag{8}$$

$$y^{'}(\varphi^{'}) = \sum_{n=1}^{N}[-na_{yn}sin(n\varphi^{'}) + nb_{yn}cos(n\varphi^{'})] \tag{9}$$

Then, the angularity of a particle can be defined as the integral of the absolute value of the change rate of θ with respect to φ, as shown in Eq. (10):

$$AI = \frac{1}{2\pi}\int_{0}^{2\pi}\left|\frac{d\theta}{d\varphi^{'}}\right|d\varphi^{'} - 1 \tag{10}$$

For a circle, it is obvious that the value of $d\theta$ is equal to the value of $d\varphi^{'}$, indicating that the angularity of a circle is actually zero. For non-circle particles, the calculation of integral would be cumbersome, and so the discretization form is more useful:

$$AI = \frac{1}{2\pi}\sum_{i=0}^{w-1}\left|\theta_{(i+1)\Delta\varphi^{'}} - \theta_{i\Delta\varphi^{'}}\right| - 1 \tag{11}$$

where w is the increment element and $\Delta\varphi^{'}$ is $2\pi/w$, i.e., the increment of polar angle. With Eq. (11), any non-circle particle can have an AI value of zero, regardless of the elongation.

(3) Roughness

Roughness (Rg) is a shape index that evaluates the concavity of the particle contour and reflects the shape difference between the real and smooth contour of particles. A Fourier transform can be used to calculate the smooth contour of a particle. The larger Fourier series (N) corresponds to a higher similarity between the real and smoothed contour [40]. In this study, the Fourier series N is set to 16 to calculate the smooth contour. The deviation between the smooth contour and the real contour is shown in Fig. 10d. Next, the deviation regions and the geometric types are extracted and determined. In the case of parts that do not intersect between the smooth contour and the actual contour, the deviation region can be calculated as a quadrilateral area (Fig. 10e). For intersecting parts, the deviation region is simplified to two triangles (Fig. 10f). At the ith microunit, the deviation distance (Δd_i) is the ratio of the deviation area to the corresponding are length. Based on the average deviation distance of all microunits, Rg can be expressed as:

$$Rg = \frac{\Delta\overline{d}}{\overline{r}} = \sqrt{\frac{\pi}{A_p}}\frac{1}{L_p}\sum_{N_d}^{i=1}A_i \tag{12}$$

where $\Delta\overline{d}$ is the average deviation distance, N_d is the number of all microunits, and A_p is the area of the particle contour. A_i is the deviation area, l_i is the corresponding arc length, and L_p is the perimeter of the particle contour.

Statistical analysis and database establishment

Through the quantification algorithms introduced above, the EI, AI, and Rg of 768 ballast particle contours, 753 cobble particle contours, and 3820 sand particle contours were calculated. The probability density distributions are shown in Fig. 11. The EI value of contours in database U_ballast satisfies the normal distribution appropriately, while

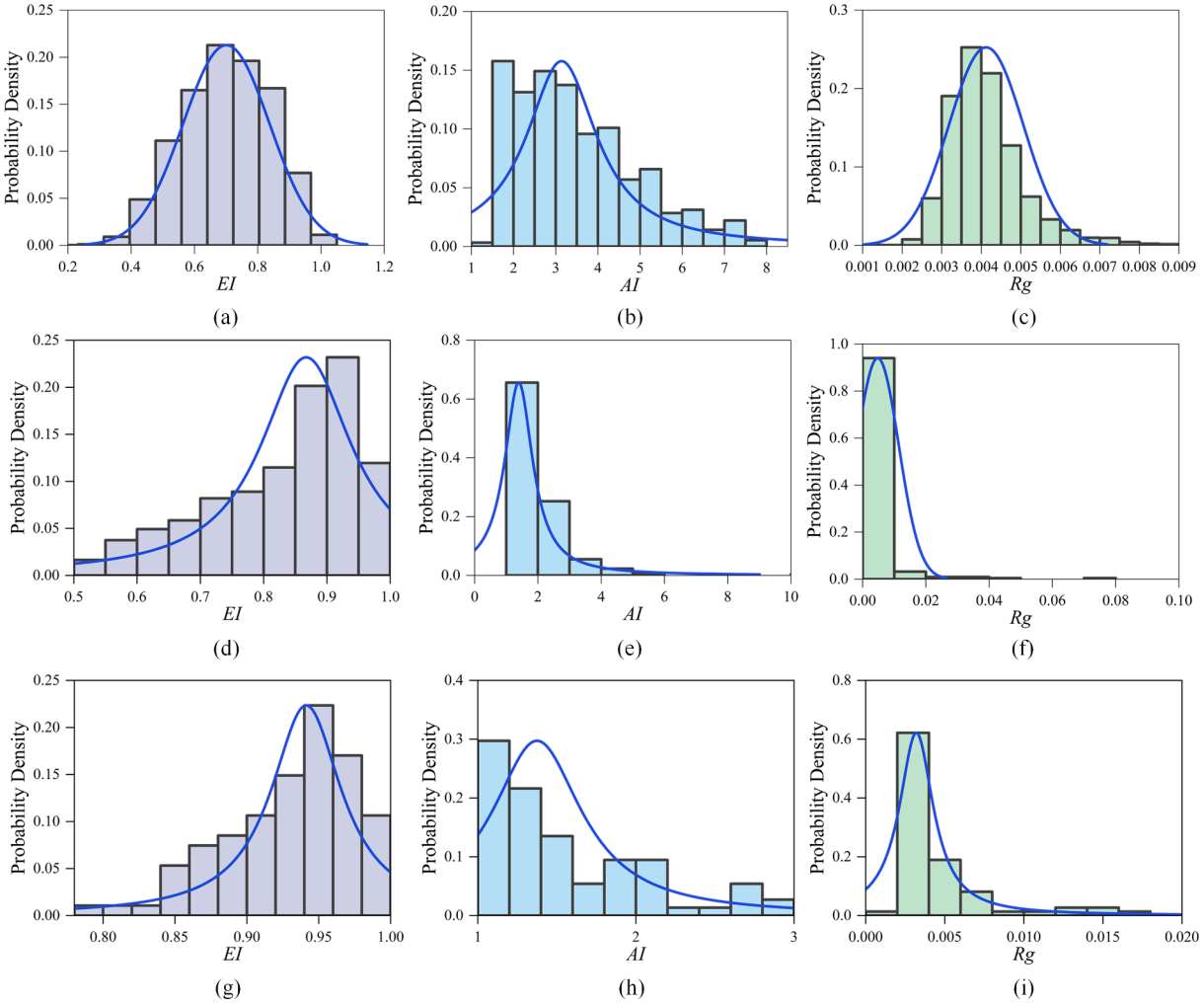

Fig. 11. Probability density distribution of the shape indexes; U_ballast: (a) EI, (b) AI, (c) Rg; U_cobble: (d) EI, (e) AI, (f) Rg; U_sand: (g) EI, (h) AI, (i)Rg

the Lorentz distribution can fit the distribution of *AI* and *Rg* of the ballast particles. For databases U_cobble and U_sand, the distribution of *EI*, *AI* and *Rg* are similar and fitted by the Lorentz distribution approximately. For example, the mean *EI* value in databases U_cobble and U_sand are 0.8807 and 0.9183, respectively, indicating that the shape in databases U_cobble and U_sand are similar to some extent.

To facilitate retrieval and sample preparation, shape indexes of U_ballast, U_cobble, and U_sand databases were stored in the form of storage format [number, contour, particle size, *EI*, *AI*, *Rg*] in the particle libraries L_B, L_C, and L_F, respectively. The steps for sample preparation from the particle databases were as follows:

(1) the required shape parameter range is input;
(2) according to the range of these values, the two-dimensional contour that meets the requirements is searched for automatically;
(3) the visualized two-dimensional contour is selected and is output to the "dxf" file.

The establishment of particle databases simplifies selecting the two-dimensional contours of GSM that meet specific requirements, thus facilitating the discrete element modeling of GSM.

DEM simulation of biaxial compression tests on realistic GSM

Two types of GSM, i.e., BSM and CSM, were employed to investigate the influence of coarse particle shape and sand content on the evolution of macroscopic and microscopic behaviors of GSM through a series of numerical biaxial compression tests using *PFC*^{2D}.

DEM modeling

Simulation process

Two groups of simulations were implemented to investigate the impact of coarse particle shape and sand content (SC) on the macroscopic and microscopic behaviors of GSM (BSM and CSM). Both coarse and fine particle shapes employed in the simulation were all selected in shape libraries L_B, L_C, and L_F stochastically. In addition, the numerical samples with SC of 0%, 10%, 20%, and 30% were selected considering the stability transition of fine particles [69]. For convenience, each sample is identified by the SC and type of mixture. For example, SC0B, SC10B, SC20B and SC30B represent BSM samples containing 0%, 10%, 20% and 30% sand, respectively. The details of each specimen are summarized in Table 1.

As illustrated in Fig. 12, the process of the numerical biaxial compressing test includes three stages [17]: (a) generation, (b) wall-servo packing, and (c) shearing. In the generation stage, particles with random orientations were initially generated in a $W \times H$ rectangular box without gravity, where $W = 0.60$ m and $H = 1.20$ m. The rectangular box was modeled with four rigid loading walls.

To guarantee accuracy and computational efficiency, the coarse particle size and fine particle size were set at 7.5 mm and 1.5 mm, respectively (Krishna and Pandey, 1981). Then, particles were subjected to an isotropic compression by a wall-servo-control mechanism to continuously adjust the positions of rigid walls until the stable confining pressure (σ_c = 200 kPa) was reached (Fig. 12c). To guarantee all samples reached the densest condition after isotropic compression, the particle friction (μ_p) and wall friction (μ_w) of zero during specimen generation was adopted based on previous studies [16]. As for the shearing stage, to exclude the influence of friction coefficient on simulation results, the particle–particle friction μ_p was set to 0.5 [9]. At the same time, the vertical loading walls moved towards each other at a rate of 0.05 to obtain a quasi-static behavior [68]. Moreover, confining pressure was applied until the axial strain of the sample reached 30% [17]. The linear elastic model was used in all modeling stages [68].

Table 1
Samples of numerical simulation.

Sample name	Sand content (%)	Material	Sample name	Sand content (%)	Material
SC0B	0	BSM	SC0C	0	CSM
SC10B	10	BSM	SC10C	10	CSM
SC20B	20	BSM	SC20C	20	CSM
SC30B	30	BSM	SC30C	30	CSM

Since the primary purpose of the simulation was focused on investigating the effect of coarse particle shapes and SC, other influencing factors, such as the micromechanical modeling parameters in DEM, were kept constant for all simulation groups. To guarantee the reasonability of the simulation, these modeling parameters were all adopted based on earlier relevant studies and are listed in Table 2. The densities of the sand and gravels were selected as 2600 kg/m^3 [62]. The normal stiffness of a sand particle and gravel particle was selected as 1×10^8 Pa, while that of the wall was set as 1×10^9 Pa [17,64]. According to Goldenberg and Goldhirsch [15], the normal-to-shear stiffness ratio of a soil particle should be selected in the range of 1.0–1.5, which can satisfy the theoretical model of the elastic sphere contact in the Cattaneo–Mindlin model [12]. In this study, the normal-to-shear stiffness ratio of a sand particle was chosen as 1.25. In addition, the damping coefficient was selected as 0.7 [75].

Variable definitions

The macroscale stress tensor computed from the microscale quantities of the contact forces and contact vectors is as follows [5]:

$$\sigma_{ij} = \frac{1}{V}\sum_{c=1}^{N_c} f_i^c d_j^c \tag{13}$$

where V is the sample volume, c represents a specific contact, N_c indicates the total number of contacts in the sample, f^c denotes the corresponding contact force, and d^c is the corresponding branch vector joining the centers of the two particles in contact. The effective mean (p') and deviatoric (q) stresses are defined as follows:

$$p' = \frac{\sigma_1 + \sigma_2}{2} \tag{14}$$

$$q = \frac{\sigma_1 - \sigma_2}{2} \tag{15}$$

where σ_1 and σ_2 represent the axial stress and lateral stress, respectively.

The internal angle of friction, φ, which indicates the shear strength of the granular material, can be defined from the stress ratio in drained biaxial loadings based on the Mohr-Coulomb criterion:

$$sin\varphi = \frac{\sigma_1 - \sigma_2}{\sigma_1 + \sigma_2} = \frac{q}{p'} \tag{16}$$

The axial strain, ε_1, and volumetric strain, ε_v, are estimated from the boundary movements:

$$\varepsilon_1 = \frac{h_0 - h}{h_0} \tag{17}$$

$$\varepsilon_v = \frac{v_0 - v}{v_0} \tag{18}$$

where h_0 and h are the initial and current heights of the sample. v_0 represents the initial volume of the sample, and v denotes the current volume of the sample.

The dilatancy angle, ψ, in the biaxial loadings is defined as follows:

$$sin\psi = -\frac{d\varepsilon_v/d\varepsilon_1}{2 - d\varepsilon_v/d\varepsilon_1} \tag{19}$$

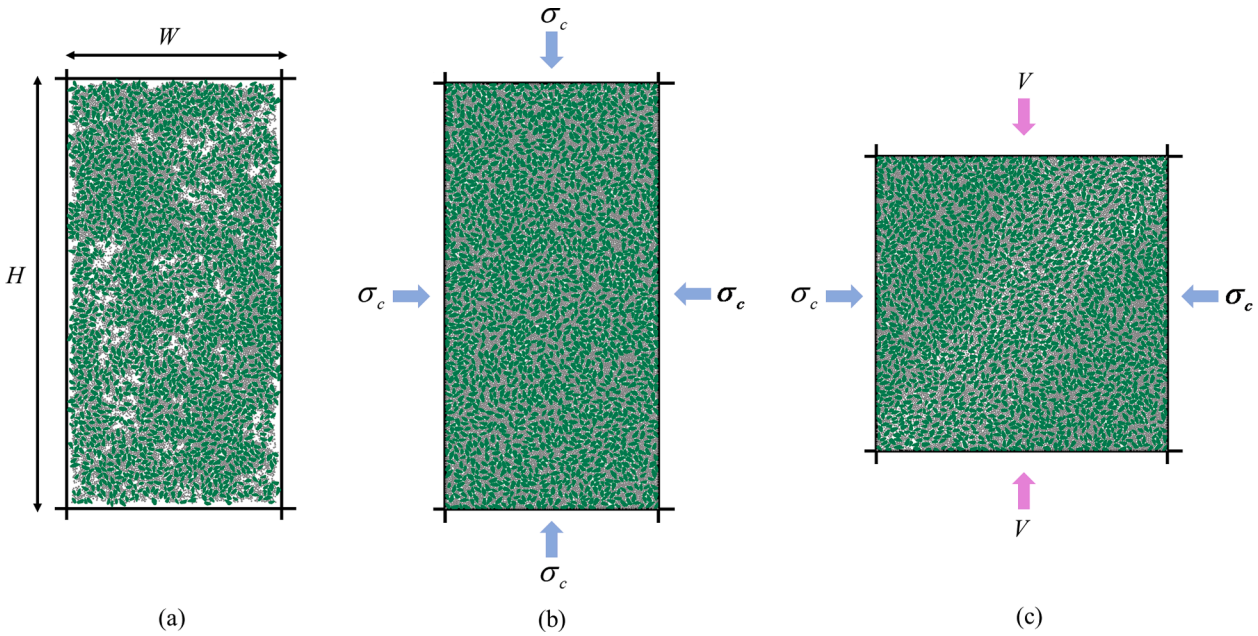

Fig. 12. Process of numerical biaxial test: (a) generation, (b) wall-servo packing, (c) shearing.

Table 2
Parameters used in the DEM simulation.

Property	Gravel particle	Sand particle	Wall
Density (kg/m^3)	2600	2600	\
Friction coefficient, μ_p	0.5	0.5	\
Normal stiffness, Pa	1×10^8	1×10^8	1×10^9
Normal-to-shear stiffness ratio	1.25	1.25	1.25
Damping coefficient	0.7	0.7	0.7

Macroscopic behaviors

Shear strength

The critical state is a physically observed state of granular materials at failure, which is an essential concept in geotechnical engineering [7]. To explore the macroscopic and microscopic behaviors at the critical state, the variation of friction angle ϕ versus the axial strain ε_1 for samples with different sand content (SC) are plotted in Fig. 13. It is clear that all samples exhibit a conventional variation with a sharp roar at the beginning and then decrease gradually and eventually approach the critical state. Furthermore, the influence of shape on stiffness is not apparent. However, ballast particle shape (angular) has a more significant influence on shear strength than sand-like cobble particle shape. The peak and residual strength of BSM decrease with the increase of SC, while the trend in CSM is not apparent.

To better identify the effect of particle shape on the shear strength, the variation of peak friction angle ϕ_p and residual friction angle ϕ_c versus the SC for samples BSM and CSM is plotted in Fig. 14. In Fig. 14a, the peak friction angle ϕ_p of BSM shows a negative relationship with SC, while that of CSM is slightly changed. Similar observations can also be found in Fig. 14b, ϕ_c of BSM drop continuously with SC while that of CSM fluctuate around 20°. The results indicate that, for the same rounded shape of sand particles, the ballast particle shape (angular) has a more significant influence on the peak strength and residual strength than that of cobble particle shape (rounded).

Volumetric strain

The variations of the volumetric strain ε_v with the axial strain ε_1 are plotted in Fig. 15. All samples experience a slight contraction before expanding gradually to plateau values. When $\varepsilon_1 \leq 5\%$, there is a positive relationship between ε_v and SC for BSM. However, at the critical state, the influence of SC on BSM is more distinct as the ε_v value of SC30B is far less than the remaining three scenarios, while the four scenarios of CSM nearly approach each other. It is noted that the ε_v increases at a low SC

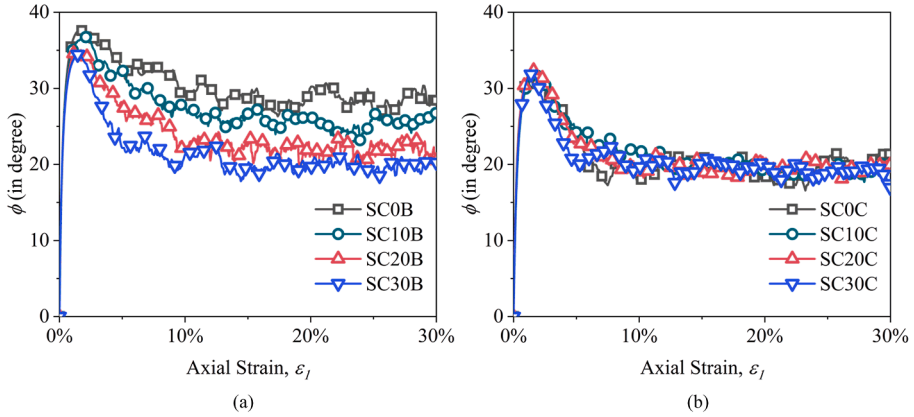

Fig. 13. Variation of friction angle ϕ versus the axial strain ε_1 for samples with different SC: (a) BSM, (b) CSM.

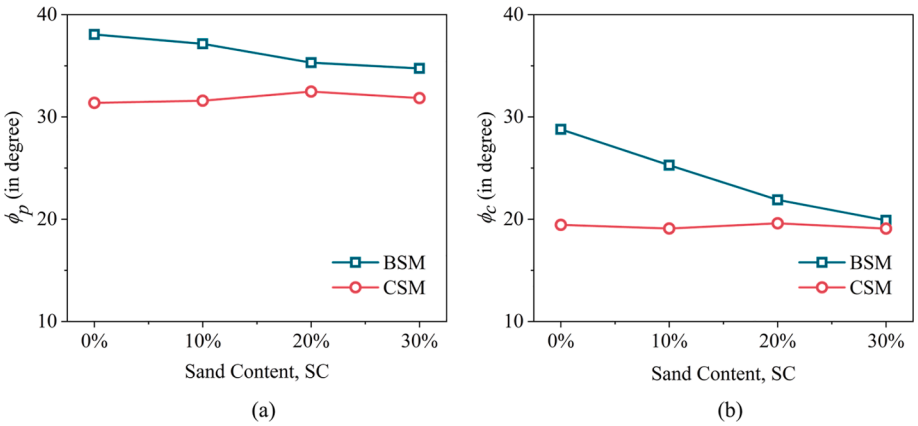

Fig. 14. Variation of peak friction angle ϕ_p and residual friction angle ϕ_c versus the SC for samples BSM and CSM: (a) peak friction angle ϕ_p, (b) residual friction angle.ϕ_c

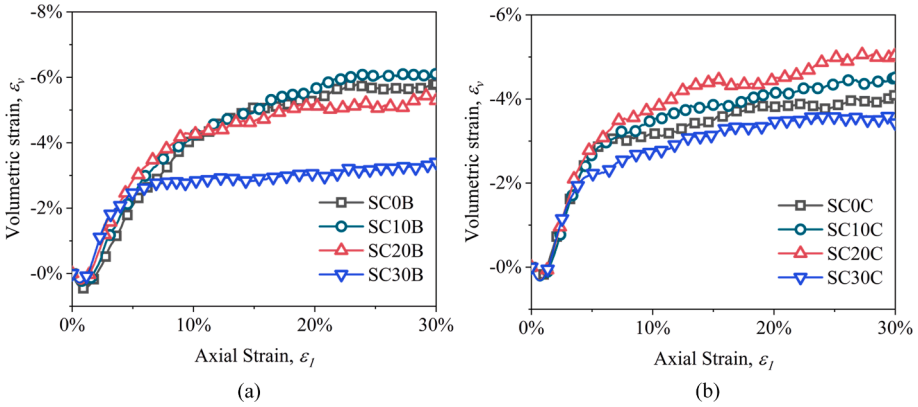

Fig. 15. Evolutions of the volumetric strain ε_v with the axial strain ε_1: (a) BSM mixtures, (b) CSM mixtures.

and decreases when SC $\geq$ 20%, suggesting that the impact of SC on dilatancy is not monotonous.

Microscopic analyses

Normal contact force and coordination number

To further investigate the interaction between different particles, three distinct types of contact was defined as gravel particle-gravel particle (GG contacts), gravel particle-sand particle (GS contacts), or sand particle-sand particle (SS contacts).

The mean normal contact force $\overline{f^n}$ is defined as the average of the normal contact forces overall contacts. In this part, the normal contact forces of each contact type at the critical states were examined in Fig. 16a and b. The sequence of contact forces: $GG > GS > SS$, was observed for all samples, which is consistent with the previous numerical studies [34,54]. In addition, for all samples, the $\overline{f^n}$ of each contact type decreases with the increase of SC.

According to Minh and Cheng [33], the coordination number Z can be defined based on the contact types:

$$Z = \frac{2N_c}{N_p}, \quad N_p = N_G + N_S \tag{20}$$

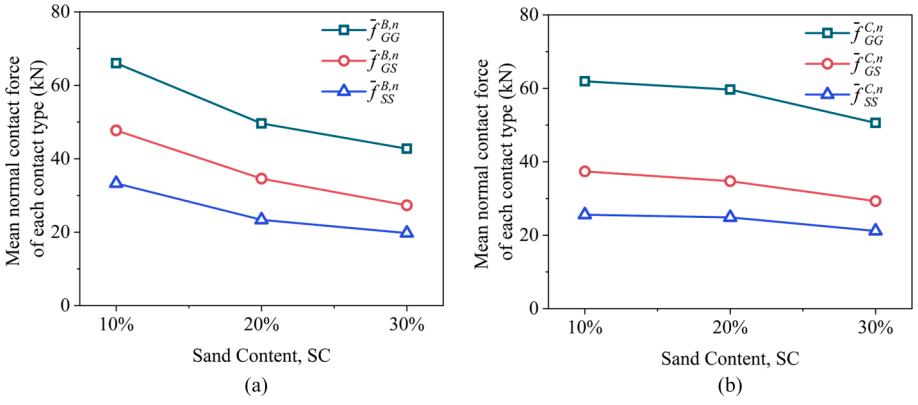

Fig. 16. Variations of the normal contact force $\overline{f^n}$ versus SC for BSM and CSM: (a) $\overline{f}^{B,n}$, (b)$\overline{f}^{C,n}$.

$$Z_{GG} = \frac{N_c^{GG}}{N_G},\ Z_{GS} = \frac{N_c^{GS}}{N_p},\ Z_{SS} = \frac{N_c^{SS}}{N_S} \tag{21}$$

where N_p, N_G, and N_S represent the number of all particles, gravel particles and sand particles, respectively. N_c^{GG}, N_c^{GS}, and N_c^{SS} are the number of *GG*, *GS*, and *SS* contacts, respectively. The variation of Z of BSM and CSM versus axial stain ε_1 are shown in Fig. 17a and b. All samples exhibit a conventional evolution with a sharp drop before gradually reaching plateau values. At the critical state, the Z values decrease with SC when SC $\leq$ 10%, while they increase with SC when SC $\geq$ 20%. This indicates that the mixture is experiencing a skeleton transition when the FC is increased from 10% to 20%.

Notably, the contact can also be classified as strong contact and weak contact. Strong contact is defined as the contact force greater than the average contact force, while weak contact carries forces smaller than the average contact force. To explore the evolution of strong and weak contacts with SC, the coordination numbers for *GG* and *SS* in strong and weak contacts of samples at the critical states are and plotted in Fig. 18. The superscripts *S* and *W* represent strong and weak contacts, respectively. For BSM and CSM, it is distinct that the Z_{GG} values show a negative linear relationship with the SC. However, Z_{SS} values exhibit a different trend, increasing significantly with the SC. As shown in Fig. 18a, the $Z_B^{GG,S}$ and $Z_B^{GG,W}$ values also decrease with the SC, opposite to the trend of $Z_B^{SS,S}$ and $Z_B^{SS,W}$. Note that the overall coordination Z_B increases with SC, indicating that the *SS* contacts gradually become dominant when SC is increased from 10% to 30%. This suggests that more mean coordination numbers of *SS* contacts are formed to support the external load when the SC is increased. Similar observations can also be found in the CSM samples. These observations suggest that the decrease of *GG* contacts and increase of *SS* contacts lead to the drop of residual shear strength with SC.

Percentage of sliding contact

In DEM simulation, the sliding of contact is governed by the Coulomb friction law. A contact sliding is assumed to occur when $|f_t|/(\mu f_n) > 0.9999$. For a specific binary mixture, the percentage of sliding contact (S_{CP}) is obtained as follows [33]:

$$S_{CP} = N_{CS}/N_C \times 100\% \tag{22}$$

where N_{CS} represents the number of sliding contacts in the sample. As shown in Fig. 19, the variation of S_{CP} soars to the peak value at approximately 1% axial strain and then plummets into a plateau value, consistent with previous studies [18]. It is evident that the S_{CP} of BSM is larger than that of CSM. This indicates that the effect of tangential contact force in BSM is larger than that of CSM under the action of external load. Additionally, S_{CP} is increased with the increase of SC for all samples. This is attributed to the rotational resistance between the nonspherical particles pushing more contacts to slide to accommodate the imposed deformations [11].

Anisotropic analysis

The direction and magnitude of contact force exhibit anisotropy, which is called contact force anisotropy characteristics. According to Sufian et al. [53], the stress tensor in Eq. (13) can be expressed in another form:

$$\sigma_{ij} = \frac{N_c}{V}\sum_m \alpha_m \int_\Omega \overline{f}_i^m(n)\overline{d}_j^m(n)E^m(n)d\Omega \tag{23}$$

where m denotes the number of subsets (i.e., $m = 3$ for GG, GS and SS subsets in this study). $\alpha_m = N_c^m/N_c$, N_c^m represents the number of contacts in the mth subset, and Ω reflects all possible orientations for a unit vector along the direction of contact normal n. $\overline{f}_i^m(n)$ is the average interparticle contact force in direction n for the mth subset and $E^m(n)$ is expressed as follows [19]:

$$E^m(n) = \frac{1}{2\pi}\left(1 + a_{ij}^{c,m} n_i n_j\right) \tag{24}$$

where $a_{ij}^{c,m}$ is the second-order anisotropy tensor, which is deviatoric and symmetric, used to characterize the fabric anisotropy.

The force anisotropy coefficient can characterize the anisotropy degree of contact force, is conventionally expressed as follows:

$$a_*^m = sign(S_r)\sqrt{\frac{a_{ij}^{*,m} a_{ij}^{*,m}}{2}} \tag{25}$$

where a_*^m including anisotropy coefficient of normal contact (a_c^m), the anisotropy coefficient of normal contact force (a_n^m), the anisotropy coefficient of tangential contact force (a_t^m), anisotropy coefficient of normal branch vector (a_{dn}^m) and anisotropy coefficient of tangential branch vector (a_{dt}^m). S_r is a normalized quantity of the double contraction of $a_{ij}^{*,m}$ and $\sigma_{ij}^{'}$.

According to Guo and Zhao [19], the integration of Eq. (23) can be expressed in this form by substituting Eq. (25):

$$\sigma_{ij} = \frac{N_c \overline{f}_0^{\,\overline{n}} d_0^{\overline{dn}}}{2V}\sum_m \varepsilon_m \left(\delta_{ij} + \frac{a_{ij}^{c,m} a_{ij}^{n,m}}{2}\delta_{ij} + \frac{a_{ij}^{c,m} + a_{ij}^{n,m} + a_{ij}^{t,m} + a_{ij}^{\mathrm{dn},m} + a_{ij}^{\mathrm{dt},m}}{2}\right) \tag{26}$$

where $\varepsilon_m = \alpha_m\gamma_m/\sum_m(\alpha_m\gamma_m)$, $\gamma_m = \frac{\overline{f}_0^{n,m}}{\overline{f}_0^{\overline{n}}}$, $\overline{f}_0^{n,m}$ denotes the average normal contact force. The effective mean ($p^{'}$) and deviatoric stresses (q) can also be defined as $p^{'} = \sigma_{ii}/2$ and $q = \sqrt{\sigma_{ij}^{'}\sigma_{ij}^{'}/2}$. Then Eq. (26) is modified into the following formula:

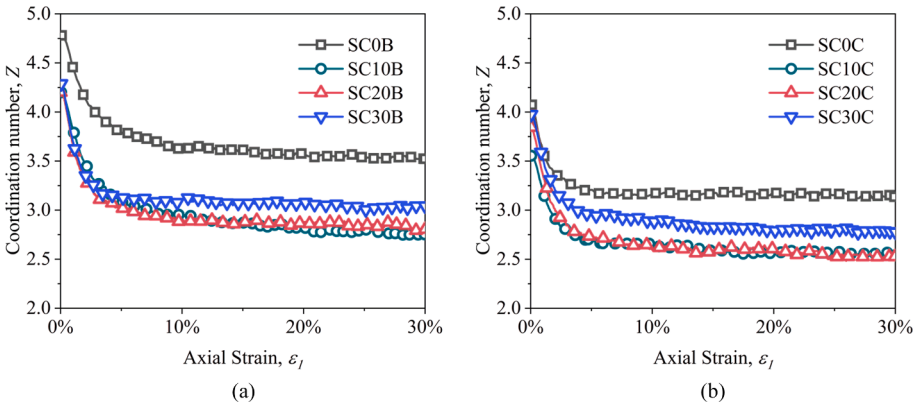

Fig. 17. Evolutions of coordination number Z versus axial strain ε_1 for BSM and CSM: (a) Z_B, (b)Z_C

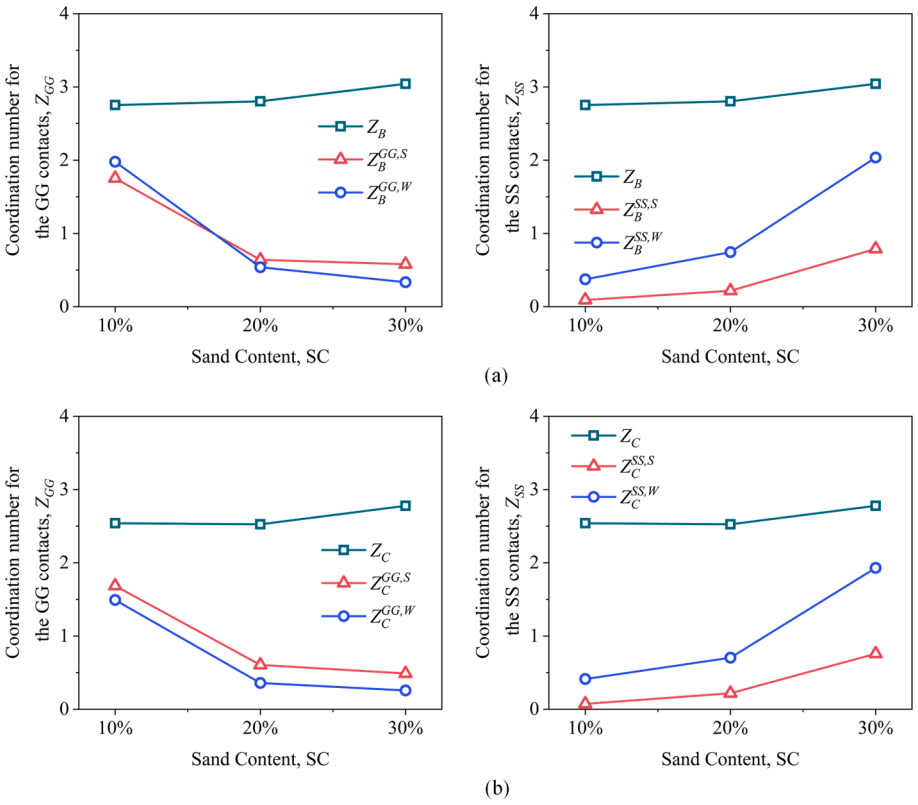

Fig. 18. Variations of the Z_{GG}, Z_{GS} and Z_{SS} with SC: (a) BSM, (b) CSM.

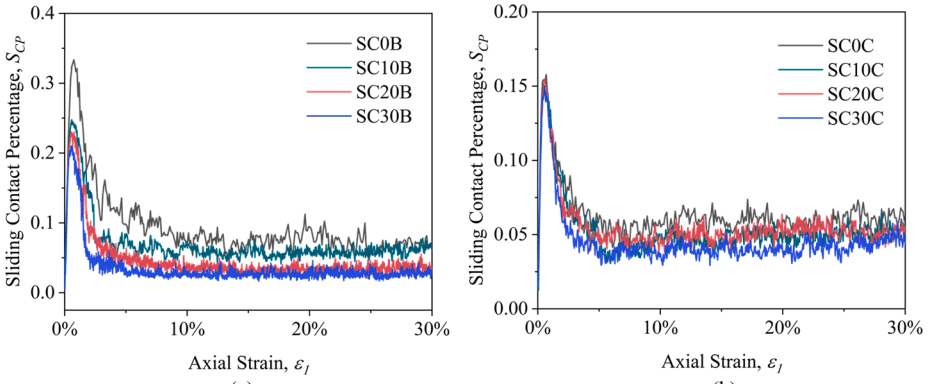

Fig. 19. Evolutions of S_{CP} with the axial strain ε_1 for BSM and CSM: (a) BSM, (b) CSM.

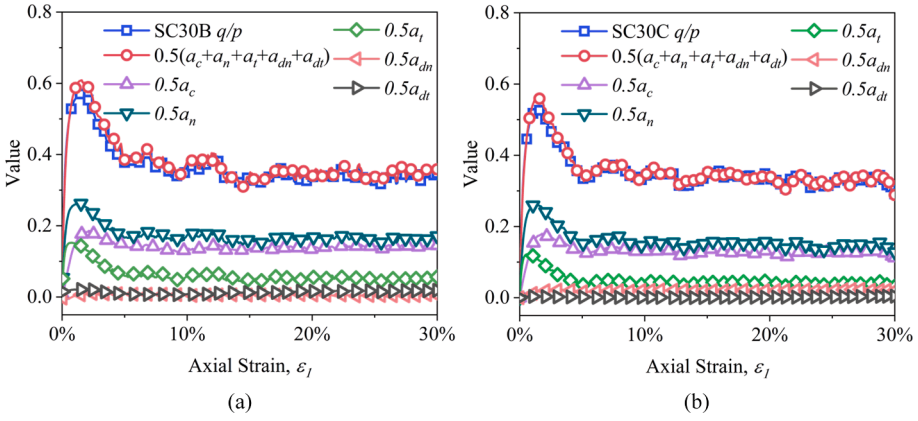

Fig. 20. The validation of Eq. (28) based on DEM data: (a) SC = 30%-B, (b) SC = 30%-C.

$$q/p^{'} = \sum_{m} \varepsilon_m \frac{\left(a_c^m + a_n^m + a_t^m + a_{\mathrm{dn}}^m + a_{\mathrm{dt}}^m\right)}{2} \tag{27}$$

Assume $\varepsilon_m = 1$, Eq. (27) for the overall contact network reduces to the following expression:

$$q/p^{'} = \frac{(a_c + a_n + a_t + a_{\mathrm{dn}} + a_{\mathrm{dt}})}{2} \tag{28}$$

To validate the relationship presented in Eq. (28), the stress ratio q/p′ obtained from DEM data based on Eq. (16) is compared with the stress ratio derived from the sources of anisotropy, as shown in Fig. 20. It is clear that the stress ratio q/p' matches the analytical expression in Eq. (28), although the analytical expression slightly underestimates q/p' at the critical state. The slight underestimation could be attributed to the fact that Eq. (28) neglects the cross products of the anisotropies [17]. This result suggests that the stress-induced anisotropies of granular materials are the microscopic origins of the shear strength. Additionally, as demonstrated in Fig. 20, a_n underpins the shear strength, a_c and a_t have secondary and tertiary contributions to the shear strength, respectively, and the contributions of a_{dn} and a_{dt} can be neglected.

To evaluate the importance of a_c, a_n, and a_t in anisotropies, the evolution of a_c, a_n, and a_t with SC are explored in Fig. 21. Clearly, a_c, a_n, and a_t of a specific SC exhibit a similar trend in evolution regardless of BSM or CSM. Specifically, a_c, a_n, and a_t initially increase sharply and then gradually drop to a plateau value except for a_c of BSM. The a_c value of SC20B and SC30B present a decrease after reaching the peak, while SC0B and SC10B still increase continuously. This suggests that the lubrication effect of fine particles in BSM can only be observed when SC > 20%. In addition, at the critical state, the value of a_c, a_n, and a_t all decrease with the increase of SC. The variations in a_c, a_n, and a_t at the critical state with respect to SC are plotted in Fig. 22. The evolutions of a_c, a_n, and a_t exhibit a similar trend, dropping with the increase of SC, expect for a_n of CSM which exhibits an increase before the drop. It is noted that the value of a_c, a_n, and a_t of BSM are always larger than that of CSM. This may be related to the fact that particle shapes affect the change of anisotropies. Based on the analysis in Fig. 22, the residual shear strength is a joint effect of a_c, a_n, and a_t. For different particle shapes of coarse particles, the ϕ_c values decrease as the SC increases, as indicated in Fig. 14b.

Conclusions

This paper proposes a systematic framework for the DEM study of realistic gravel-sand mixture from particle recognition to macro-and micro-mechanical analysis. The contour of particles was determined in this study using a deep-learning-enhanced particle identification approach with the assistance of a close-range photogrammetry system. The extracted contours were quantified by shape indexes and stored in three shape libraries. Additionally, a series of numerical biaxial compression tests were conducted to evaluate the effect of coarse particle shape and fine sand content on macroscopic and microscopic behaviors.

The major contribution of the proposed study is concluded as follows:

(1) High-quality images of GSM samples were efficiently acquired based on a novel photogrammetry system. This system consisted of a small four-axis gantry palletizing manipulator, digital camera, and computer. It provided a reliable and fast way for

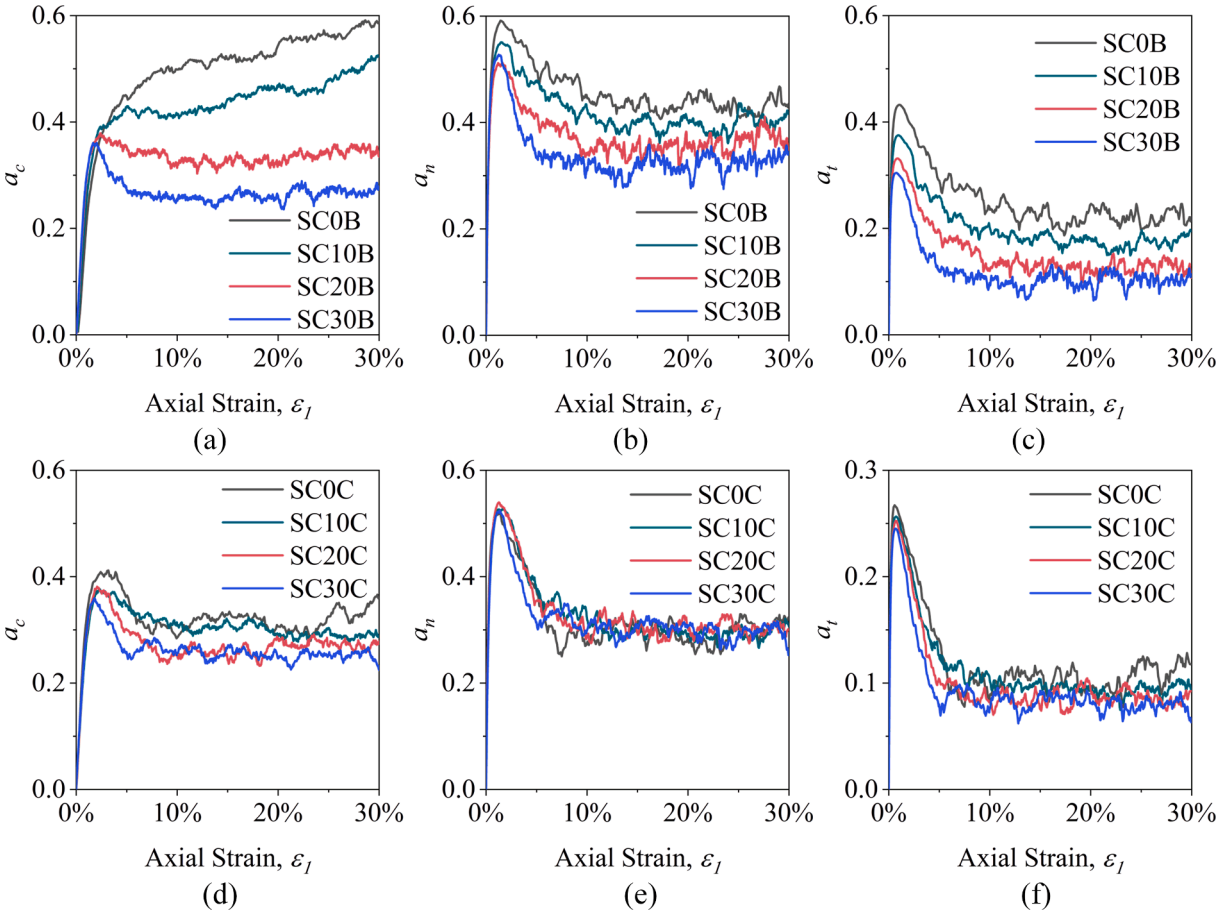

Fig. 21. Evolution of a_c, a_n, and a_t versus axial strain ε_1: (a) a_c of BSM, (b) a_n of BSM, (c) a_t of BSM, (d) a_c of CSM, (e) a_n of CSM, (f) a_t of CSM.

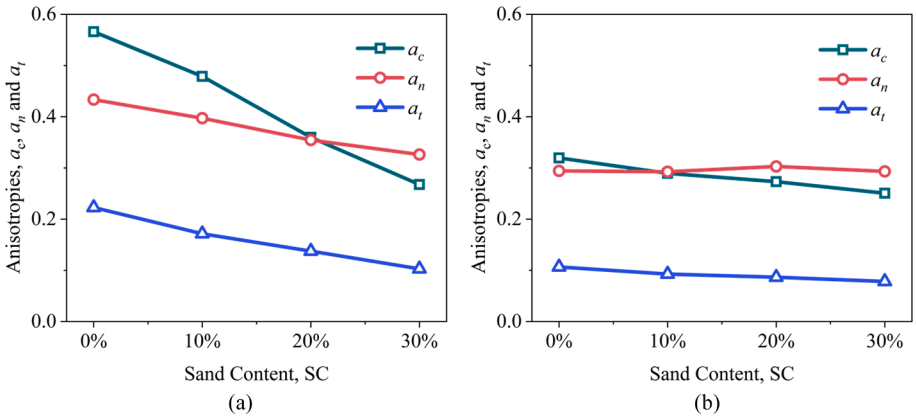

Fig. 22. Variarion of a_c, a_n and a_t with respect to SC: (a) B SM, (b) CSM.

obtaining original sample images automatically, which could be used for image acquisition in other conventional samples.

(2) Three training data sets Y_ballast, Y_cobble, and Y_sand were established, for ballast particle images, cobble particle images, and sand particle images, respectively. The YOLOv5 was employed to distinguish the location of full-projection particles of varying sizes in the above data sets and generate three data sets D_ballast, D_cobble, and D_sand for training of the U-Net model. Particle shapes were recognized accurately through the trained U-Net model and stored in U_ballast, U_cobble, and U_sand data sets. All these training set databases could be further expanded, and the trained model could be modified to identify more different kinds of particles in the future.

(3) The recognized particle contours were evaluated by three typical shape indexes (elongation, angularity index, and roughness), and the results were stored in shape databases L_B, L_C, and L_F, respectively. The particle shapes could be imported into the DEM simulation conveniently through specific retrieval.

(4) Based on a series DEM simulation, the particle shape of coarse particles was found to influence the mechanical properties of the gravel-sand mixture significantly. Specifically, the sample with ballast particle shape had a higher peak strength and residual strength than that with cobble particle shape. In addition, the influence of sand content on the mechanical properties of granular materials was not monotonous. When SC ranges from 10% to 20%, the mixture might experience a skeleton transition. When SC $>$ 20%, the lubricating role of sand particles would be observed.

The author acknowledged that the shape features obtained from 2D extraction still differ from 3D particle shape features. Therefore, the current proposed framework will be further extended into 3D. In this way, a voxel-based deep learning neural network will be built to reproduce the 3D particle shapes and microstructures based on the CT-obtained voxel images. Additionally, a 3D DEM simulation will be performed using realistic three-dimensional clump particles. Indeed, the proposed research paves a viable way to investigate various granular mixture materials in DEM simulations.

CRediT authorship contribution statement

Ruidong Li: Methodology, Formal analysis, Writing – original draft. **Xiangyu Hu:** Software, Writing – review & editing. **Fan Chen:** Data curation. **Xiang Wang:** Conceptualization, Supervision, Writing – review & editing, Project administration. **Hao Xiong:** Data curation, Visualization, Writing – review & editing. **Hao Wu:** Investigation, Writing – review & editing.

Declaration of Competing Interest

The authors declare that they have no known competing financial interests or personal relationships that could have appeared to influence the work reported in this paper.

Acknowledgments

The study was supported by the National Natural Science Foundation of China (Nos. 51978674 and 52090084). The authors appreciate this financial assistance.

References

[1] Bai H, Li R, Hu X, Chen F, Liao Z, Yao Y. Automated Shape Analysis and DEM Study on Graded Crushed Stone. Adv Mater Sci Eng 2021;2021:1–14. https://doi.org/10.1155/2021/3463363.
[2] Bai H, Li R, Wang W, Xie K, Wang X, Zhang W. Investigation on Parameter Calibration Method and Mechanical Properties of Root-Reinforced Soil by DEM. Math Probl Eng 2021;2021:1–18. https://doi.org/10.1155/2021/6623489.
[3] Barrett PJ. The shape of rock particles, a critical review. Sedimentology 1980;27(3):291–303. https://doi.org/10.1111/j.1365-3091.1980.tb01179.x.
[4] Bochkovskiy A, Wang C-Y, Liao H-YM. YOLOv4: Optimal Speed and Accuracy of Object Detection. ArXiv200410934 Cs Eess; 2020.
[5] Christoffersen J, Mehrabadi MM, Nemat-Nasser S. A Micromechanical Description of Granular Material Behavior. J Appl Mech 1981;48:339–44. https://doi.org/10.1115/1.3157619.
[6] Cundall PA, Strack ODL. A discrete numerical model for granular assemblies. Géotechnique 1979;29(1):47–65. https://doi.org/10.1680/geot.1979.29.1.47.
[7] Dafalias YF. Must critical state theory be revisited to include fabric effects? Acta Geotech 2016;11(3):479–91. https://doi.org/10.1007/s11440-016-0441-0.
[8] Danesh A, Mirghasemi AA, Palassi M. Evaluation of particle shape on direct shear mechanical behavior of ballast assembly using discrete element method (DEM). Transp Geotech 2020;23:100357. https://doi.org/10.1016/j.trgeo.2020.100357.
[9] de Frias Lopez R, Ekblad J, Silfwerbrand J. Resilient properties of binary granular mixtures: A numerical investigation. Comput Geotech 2016;76:222–33. https://doi.org/10.1016/j.compgeo.2016.03.002.
[10] Deng R, Shen C, Liu S., Wang H, Liu X. Learning to predict crisp boundaries. ArXiv180710097 Cs; 2018.
[11] Estrada N, Azéma E, Radjai F, Taboada A. Identification of rolling resistance as a shape parameter in sheared granular media. Phys Rev E 2011;84:011306. https://doi.org/10.1103/PhysRevE.84.011306.
[12] Fischer-Cripps AC. Introduction to contact mechanics. Mechanical engineering series. 2nd ed. New York: Springer; 2007.
[13] Furukawa Y, Ponce J. Accurate Camera Calibration from Multi-View Stereo and Bundle Adjustment. Int J Comput Vis 2009;84(3):257–68. https://doi.org/10.1007/s11263-009-0232-2.
[14] Golab L, DeHaan D, Demaine ED, Lopez-Ortiz A, Munro JI. Identifying frequent items in sliding windows over on-line packet streams. In: Proceedings of the 2003 ACM SIGCOMM Conference on Internet Measurement - IMC '03. Presented at the the 2003 ACM SIGCOMM conference. Miami Beach, FL, USA: ACM Press; 2003. p. 173. https://doi.org/10.1145/948205.948227.
[15] Goldenberg C, Goldhirsch I. Friction enhances elasticity in granular solids. Nature 2005;435(7039):188–91. https://doi.org/10.1038/nature03497.
[16] Gong J, Liu J. Mechanical transitional behavior of binary mixtures via DEM: Effect of differences in contact-type friction coefficients. Comput Geotech 2017;85:1–14. https://doi.org/10.1016/j.compgeo.2016.12.009.

[17] Gong J, Nie Z, Zhu Y, Liang Z, Wang X. Exploring the effects of particle shape and content of fines on the shear behavior of sand-fines mixtures via the DEM. Comput Geotech 2019;106:161–76. https://doi.org/10.1016/j.compgeo.2018.10.021.
[18] Gu X, Huang M, Qian J. DEM investigation on the evolution of microstructure in granular soils under shearing. Granul Matter 2014;16(1):91–106. https://doi.org/10.1007/s10035-013-0467-z.
[19] Guo N, Zhao J. The signature of shear-induced anisotropy in granular media. Comput Geotech 2013;47:1–15. https://doi.org/10.1016/j.compgeo.2012.07.002.
[20] Iannacchione AT, Vallejo LE. Shear Strength Evaluation of Clay-Rock Mixtures. In: Slope Stability 2000. Presented at the Geo-Denver 2000. Denver, Colorado, United States: American Society of Civil Engineers; 2000. p. 209–23. https://doi.org/10.1061/40512(289)16.
[21] Jensen RP, Edil TB, Bosscher PJ, Plesha ME, Kahla NB. Effect of Particle Shape on Interface Behavior of DEM-Simulated Granular Materials. Int J Geomech 2001;1(1):1–19. https://doi.org/10.1061/(ASCE)1532-3641(2001)1:1(1).
[22] Ji X, Han Bo, Hu J, Li S, Xiong Y, Sun E. Application of the discrete element method and CT scanning to investigate the compaction characteristics of the soil–rock mixture in the subgrade. Road Mater Pavement Des 2022;23(2):397–413. https://doi.org/10.1080/14680629.2020.1826350.
[23] Jiang G-L, Tatsuoka F, Flora A, Koseki J. Inherent and stress-state-induced anisotropy in very small strain stiffness of a sandy gravel. Géotechnique 1997;47(3):509–21. https://doi.org/10.1680/geot.1997.47.3.509.
[24] Orford JD, Carter RWG. Crestal Overtop and Washover Sedimentation on a Fringing Sandy Gravel Barrier Coast, Carnsore Point. Southeast Ireland SEPM J Sediment Res 1982;52. https://doi.org/10.1306/212F7F2C-2B24-11D7-8648000102C1865D.
[25] Kingma DP, Ba J. Adam: A Method for Stochastic Optimization. ArXiv14126980 Cs; 2017.
[26] Kuznetsova A, Maleva T, Soloviev V. Detecting Apples in Orchards Using YOLOv3 and YOLOv5 in General and Close-Up Images. In: Han M, Qin S, Zhang N, editors. Advances in Neural Networks – ISNN 2020 Lecture Notes in Computer Science. Cham: Springer International Publishing; 2020. p. 233–43. https://doi.org/10.1007/978-3-030-64221-1_20.
[27] Li XQ, Chen Z, Zhang LT, Jia D. Construction and Accuracy Test of a 3D Model of Non-Metric Camera Images Using Agisoft PhotoScan. Procedia Environ Sci 2016;36:184–90. https://doi.org/10.1016/j.proenv.2016.09.031.
[28] Liang Z, Nie Z, An A, Gong J, Wang X. A particle shape extraction and evaluation method using a deep convolutional neural network and digital image processing. Powder Technol 2019;353:156–70. https://doi.org/10.1016/j.powtec.2019.05.025.
[29] Lienhart R, Maydt J. An extended set of Haar-like features for rapid object detection. In: Proceedings. International Conference on Image Processing. Presented at the ICIP 2002 International Conference on Image Processing,. Rochester, NY, USA: IEEE; 2002. I-900–3. https://doi.org/10.1109/ICIP.2002.1038171.
[30] Liu J, Wang P, Liu J. Macro- and micro-mechanical characteristics of crushed rock aggregate subjected to direct shearing. Transp Geotech 2015;2:10–9. https://doi.org/10.1016/j.trgeo.2014.07.007.
[31] Masad E, Olcott D, White T, Tashman L. Correlation of Fine Aggregate Imaging Shape Indices with Asphalt Mixture Performance. Transp Res Rec J Transp Res Board 2001;1757(1):148–56. https://doi.org/10.3141/1757-17.
[32] Meng QX, Wang HL, Xu WY, Cai M. A numerical homogenization study of the elastic property of a soil-rock mixture using random mesostructure generation. Comput Geotech 2018;98:48–57. https://doi.org/10.1016/j.compgeo.2018.01.015.
[33] Minh NH, Cheng YP. A DEM investigation of the effect of particle-size distribution on one-dimensional compression. Géotechnique 2013;63(1):44–53. https://doi.org/10.1680/geot.10.P.058.
[34] Minh NH, Cheng YP, Thornton C. Strong force networks in granular mixtures. Granul Matter 2014;16(1):69–78. https://doi.org/10.1007/s10035-013-0455-3.
[35] Mizuno K, Terachi Y, Takagi K, Izumi S, Kawaguchi H, Yoshimoto M. Architectural Study of HOG Feature Extraction Processor for Real-Time Object Detection. In: 2012 IEEE Workshop on Signal Processing Systems. Presented at the 2012 IEEE Workshop on Signal Processing Systems (SiPS). Quebec City, QC: IEEE; 2012. p. 197–202. https://doi.org/10.1109/SiPS.2012.57.
[36] Nardi L, Rinaldi M, Solari L. An experimental investigation on mass failures occurring in a riverbank composed of sandy gravel. Geomorphology 2012;163–164:56–69. https://doi.org/10.1016/j.geomorph.2011.08.006.
[37] Ng T-T, Zhou W, Chang X-L. Effect of Particle Shape and Fine Content on the Behavior of Binary Mixture. J Eng Mech 2017;143(1). https://doi.org/10.1061/(ASCE)EM.1943-7889.0001070.
[38] Nguyen HBK, Rahman MM, Fourie AB. Effect of Particle Shape on Constitutive Relation: DEM Study. J Geotech Geoenvironmental Eng 2020;146(7):04020058. https://doi.org/10.1061/(ASCE)GT.1943-5606.0002278.
[39] Nie Z-H, Wang X, Huang D-L, Zhao L-H. Fourier-shape-based reconstruction of rock joint profile with realistic unevenness and waviness features. J Cent South Univ 2019;26(11):3103–13. https://doi.org/10.1007/s11771-019-4239-8.
[40] Nie Z, Zhu Y, Wang X, Gong J. Investigating the effects of Fourier-based particle shape on the shear behaviors of rockfill material via DEM. Granul Matter 2019;21:22. https://doi.org/10.1007/s10035-019-0875-9.
[41] Oskooei PR, Mohammadinia A, Arulrajah A, Horpibulsuk S. DEM modeling and experimental analysis of the breakage behavior of recycled crushed brick particles. Transp Geotech 2021;30:100586. https://doi.org/10.1016/j.trgeo.2021.100586.
[42] Pun WK, Cheung WM, Lui LS. Geotechnical standards in Hong Kong, in: New Generation Design Codes for Geotechnical Engineering Practice — Taipei 2006. In: Presented at the Proceedings of the International Symposium. Taipei, Taiwan: WORLD SCIENTIFIC, National Taiwan University of Science and Technology; 2006. https://doi.org/10.1142/9789812772480_0014.
[43] Qian J, Yao Y, Li J, Xiao H, Luo S. Resilient Properties of Soil-Rock Mixture Materials: Preliminary Investigation of the Effect of Composition and Structure. Materials 2020;13:1658. https://doi.org/10.3390/ma13071658.
[44] Rahman S, Khattak MJ, Adhikari B, Adhikari S. Discrete element modeling of bonded soil mixtures under uniaxial compression and indirect tension test. Transp Geotech 2021;26:100438. https://doi.org/10.1016/j.trgeo.2020.100438.
[45] Ronneberger O, Fischer P, Brox T. U-Net: Convolutional Networks for Biomedical Image Segmentation. In: Navab N, Hornegger J, Wells WM, Frangi AF, editors. Medical Image Computing and Computer-Assisted Intervention – MICCAI 2015, Lecture Notes in Computer Science. Cham: Springer International Publishing; 2015. p. 234–41. https://doi.org/10.1007/978-3-319-24574-4_28.
[46] Sandeep CS, Li S, Senetakis K. Scale and surface morphology effects on the micromechanical contact behavior of granular materials. Tribol Int 2021;159:106929. https://doi.org/10.1016/j.triboint.2021.106929.
[47] Sandeep CS, Senetakis K. An experimental investigation of the microslip displacement of geological materials. Comput Geotech 2019;107:55–67. https://doi.org/10.1016/j.compgeo.2018.11.013.
[48] Sandeep CS, Senetakis K. Influence of morphology on the micro-mechanical behavior of soil grain contacts. Geomech Geophys Geo-Energy Geo-Resour 2019;5(2):103–19. https://doi.org/10.1007/s40948-018-0094-6.
[49] Seitz SM, Curless B, Diebel J, Scharstein D, Szeliski R. A Comparison and Evaluation of Multi-View Stereo Reconstruction Algorithms. In: 2006 IEEE Computer Society Conference on Computer Vision and Pattern Recognition - Volume 1 (CVPR'06). Presented at the 2006 IEEE Computer Society Conference on Computer Vision and Pattern Recognition - Volume 1 (CVPR'06). New York, NY, USA: IEEE; 2006. p. 519–28. https://doi.org/10.1109/CVPR.2006.19.
[50] Spettl A, Bachstein S, Dosta M, Goslinska M, Heinrich S, Schmidt V. Bonded-particle extraction and stochastic modeling of internal agglomerate structures. Adv Powder Technol 2016;27(4):1761–74. https://doi.org/10.1016/j.apt.2016.06.007.
[51] Stojmenović M, Žunić J. Measuring Elongation from Shape Boundary. J Math Imaging Vis 2008;30(1):73–85. https://doi.org/10.1007/s10851-007-0039-0.
[52] Strahler A, Stuedlein AW, Arduino PW. Stress-Strain Response and Dilatancy of Sandy Gravel in Triaxial Compression and Plane Strain. J Geotech Geoenviron Eng 2016;142(4):04015098. https://doi.org/10.1061/(ASCE)GT.1943-5606.0001435.
[53] Sufian A, Russell AR, Whittle AJ. Anisotropy of contact networks in granular media and its influence on mobilised internal friction. Géotechnique 2017:1–14. https://doi.org/10.1680/jgeot.16.P.170.
[54] Voivret C, Radjaï F, Delenne J-Y, El Youssoufi MS. Multiscale Force Networks in Highly Polydisperse Granular Media. Phys Rev Lett 2009;102:178001. https://doi.org/10.1103/PhysRevLett.102.178001.
[55] Wang S, Chen G, Zhang L, Yuan J. Triaxial Discrete Element Simulation of Soil-Rock Mixture with Different Rock Particle Shapes under Rigid and Flexible Loading Modes. Int J Geomech 2021;21(8):04021142. https://doi.org/10.1061/(ASCE)GM.1943-5622.0002081.
[56] Wang X, Yin Z, Xiong H, Su D, Feng Y. A spherical-harmonic-based approach to discrete element modeling of 3D irregular particles. Int J Numer Methods Eng 2021;122:5626–55. https://doi.org/10.1002/nme.6766.
[57] Wang X, Yin Z-Y, Su D, Wu X, Zhao J. A novel approach of random packing generation of complex-shaped 3D particles with controllable sizes and shapes. Acta Geotech 2021. https://doi.org/10.1007/s11440-021-01155-3.
[58] Wang X, Yin Z-Y, Su D, Xiong H, Feng YT. A novel Arcs-based discrete element modeling of arbitrary convex and concave 2D particles. Comput Methods Appl Mech Eng 2021;386:114071. https://doi.org/10.1016/j.cma.2021.114071.
[59] Wang Y, Li CH, Hu YZ. Use of X-ray computed tomography to investigate the effect of rock blocks on meso-structural changes in soil-rock mixture under triaxial deformation. Constr Build Mater 2018;164:386–99. https://doi.org/10.1016/j.conbuildmat.2017.12.173.
[60] Wang Y, Li X. Experimental study on cracking damage characteristics of a soil and rock mixture by UPV testing. Bull Eng Geol Environ 2015;74(3):775–88. https://doi.org/10.1007/s10064-014-0673-x.
[61] Wettimuny R, Penumadu D. Application of Fourier Analysis to Digital Imaging for Particle Shape Analysis. J Comput Civ Eng 2004;18(1):2–9. https://doi.org/10.1061/(ASCE)0887-3801(2004)18:1(2).
[62] Xu D-S, Tang J-Y, Zou Y, Rui R, Liu H-B. Macro and micro investigation of gravel content on simple shear behavior of sand-gravel mixture. Constr Build Mater 2019;221:730–44. https://doi.org/10.1016/j.conbuildmat.2019.06.091.
[63] Xu W-J, Hu L-M, Gao W. Random generation of the meso-structure of a soil-rock mixture and its application in the study of the mechanical behavior in a landslide dam. Int J Rock Mech Min Sci 2016;86:166–78. https://doi.org/10.1016/j.ijrmms.2016.04.007.
[64] Yang Y, Wang JF, Cheng YM. Quantified evaluation of particle shape effects from micro-to-macro scales for non-convex grains. Particuology 2016;25:23–35. https://doi.org/10.1016/j.partic.2015.01.008.
[65] Yin Z-Y, Wang P. Micro-mechanical analysis of caisson foundation in sand using DEM: Particle shape effect. Appl Ocean Res 2021;111:102630. https://doi.org/10.1016/j.apor.2021.102630.
[66] Yin Z-Y, Wang P, Zhang F. Effect of particle shape on the progressive failure of shield tunnel face in granular soils by coupled FDM-DEM method. Tunn Undergr Space Technol 2020;100:103394. https://doi.org/10.1016/j.tust.2020.103394.
[67] Yongbo F, Adewuyi OI, Chun F. Strength characteristics of soil rock mixture under equal stress and cyclic loading conditions. Geosystem Eng 2015;18(1):73–7. https://doi.org/10.1080/12269328.2014.1002633.

[68] Zhang J, Wang X, Yin Z-Y, Liang Z. DEM modeling of large-scale triaxial test of rock clasts considering realistic particle shapes and flexible membrane boundary. Eng Geol 2020;279:105871. https://doi.org/10.1016/j.enggeo.2020.105871.
[69] Zhang J, Chen X, Zhang J, Wang X. Microscopic investigation of the packing features of soft-rigid particle mixtures using the discrete element method. Adv Powder Technol 2020;31(7):2951–63. https://doi.org/10.1016/j.apt.2020.05.019.
[70] Zhang P, Yin Z-Y. A novel deep learning-based modelling strategy from image of particles to mechanical properties for granular materials with CNN and BiLSTM. Comput Methods Appl Mech Eng 2021;382:113858. https://doi.org/10.1016/j.cma.2021.113858.
[71] Zheng Z, Wang P, Liu W, Li J, Ye R, Ren D. Distance-IoU Loss: Faster and Better Learning for Bounding Box Regression. Proc AAAI Conf Artif Intell 2020;34:12993–3000. https://doi.org/10.1609/aaai.v34i07.6999.
[72] Zhou Bo, Ku Q, Wang H, Wang J. Particle classification and intra-particle pore structure of carbonate sands. Eng Geol 2020;279:105889. https://doi.org/10.1016/j.enggeo.2020.105889.
[73] Zhou B, Wang J, Wang H. Three-dimensional sphericity, roundness and fractal dimension of sand particles. Géotechnique 2018;68(1):18–30. https://doi.org/10.1680/jgeot.16.P.207.
[74] Zhou B, Wang J, Zhao B. Micromorphology characterization and reconstruction of sand particles using micro X-ray tomography and spherical harmonics. Eng Geol 2015;184:126–37. https://doi.org/10.1016/j.enggeo.2014.11.009.
[75] Zhu Y, Nie Z, Gong J, Zou J, Zhao L, Li L. An analysis of the effects of the size ratio and fines content on the shear behaviors of binary mixtures using DEM. Comput Geotech 2020;118:103353. https://doi.org/10.1016/j.compgeo.2019.103353.